SPIN90 modulates the architecture of lamellipodial actin in an ARPC5L dependent fashion.

LuYan Cao[1,2*], Angika Basant[1†], Miroslav Mladenov[1], Naoko Kogata[1], Antoine Jegou[2], Guillaume Romet-Lemonne[2], Sophie Brasselet[3], Manos Mavrakis[3], Michael Way[1,4*]

1. The Francis Crick Institute, 1 Midland Road, London, NW1 1AT, UK.
2. Université Paris Cité, CNRS, Institut Jacques Monod, 75013 Paris, France.
3. Institut Fresnel, CNRS UMR7249, Aix Marseille Univ, Centrale Med, 13013 Marseille, France
4. Department of Infectious Disease, Imperial College, London W2 1PG, UK.

[†] Current address: King's College London, Guy's Campus, London, SE1 1UL, UK

* Joint corresponding authors: luyan.cao@ijm.fr; michael.way@crick.ac.uk

Abstract

When stimulated by nucleation-promoting factors such as WAVE, the Arp2/3 complex generates branched actin networks. In contrast, when activated by SPIN90, the Arp2/3 complex generates linear actin filaments. The Arp2/3 complex in mammals, consists of 8 iso-complexes with different properties as there are two isoforms of Arp3, ArpC1 and ArpC5. Here, using recombinant Arp2/3 iso-complexes with defined compositions, we show that SPIN90 selectively activates ArpC5L- rather than ArpC5- containing complexes to generate linear actin filaments. Consistent with this, SPIN90 at the leading edge of migrating cells enhances the recruitment of ArpC5L-, but not ArpC5- containing, Arp2/3 complexes to lamellipodia. These SPIN90-Arp2/3-ArpC5L complexes generate linear actin filaments that integrate into lamellipodia and impact protrusion efficiency. Moreover, using polarised light microscopy, we show that loss of SPIN90 leads to an enrichment in actin filaments oriented more perpendicular to the plasma membrane. Our results demonstrate that SPIN90 regulates the architecture and dynamics of lamellipodial actin in an Arp2/3 iso-complex dependent fashion.

Summary

SPIN90 selectively recruits and activates ArpC5L containing Arp2/3 to shape the architecture and dynamics of lamellipodial actin.

Introduction

Highly conserved throughout evolution, the Arp2/3 complex is a unique actin nucleator, essential for generating branched actin networks [1-4]. Consequently, the Arp2/3 complex is an important regulator of the architecture and dynamics of the actin cytoskeleton [5-9]. Activated by class I nucleation-promoting factors (NPFs), such as WAVE, N-WASP, WASP, and WASH, the Arp2/3 complex can bind to pre-existing actin filaments, also known as mother filaments, and initiate the formation of a new actin branch, or a daughter filament [9-11]. Alternatively, when activated by SPIN90 (also known as WISH, NCKIPSD, or Dip1), the Arp2/3 complex is unable to bind to an existing actin filament and rather generates a new linear actin filament [8,12]. Given its ability to nucleate actin networks, the Arp2/3 complex is indispensable for various cellular functions, including endocytosis, cell migration, and DNA repair [2,13-17]. Among these processes, SPIN90–Arp2/3 contributes to the initiation of yeast endocytosis by providing the actin filaments required for actin branch formation [8] and in the regulation of mammalian cortical actin by tuning its architecture [13,18].

The Arp2/3 complex contains seven subunits, the Actin Related Proteins Arp2 and Arp3, as well as ArpC1-ArpC5 [1,3,19]. In higher eukaryotes, such as mammals, there are two isoforms of Arp3, ArpC1, and ArpC5, encoded by distinct genes [1,20,21]. In humans, Arp3 and Arp3B are 91% identical, while ArpC1A/ArpC1B and ArpC5/ArpC5L each share 67% identity [22]. These different subunit isoforms have been shown to give the Arp2/3 complex distinct cellular and physiological functions [11,23-25]. In addition, mutations in human ArpC1B cause severe inflammation and immunodeficiency [26,27]. Loss of ArpC5 also leads to multiple congenital deficiencies, inflammation, dysregulated host-microbiome interactions, and increased mortality [28-30].

To understand the molecular mechanism underlying these phenotypes, it is essential to dissect the properties of the different Arp2/3 iso-complexes. Arp2/3 iso-complexes have subtly but recognizably different structural conformations [25,31,32] and respond differently to the widely used Arp2/3 inhibitors, CK-666 and CK-869 [33]. Previous studies have also shown that all Arp2/3 iso-complexes, regardless of their subunit composition, can generate actin branches. Complexes containing ArpC1B or ArpC5L are, however, more efficient at branch formation than those with ArpC1A or ArpC5 [22], while networks generated by Arp3B-containing complexes disassemble faster than those formed by Arp3-containing complexes in cells due to oxidation of Methionine 293 of Arp3B by MICAL2 [34].

In contrast, it is still unclear whether all Arp2/3 iso-complexes generate linear actin filaments when activated by SPIN90. In particular, our previous work demonstrated that although CK-666 inhibits all Arp2/3 iso-complexes from generating linear filaments, it only blocks ArpC1A containing complexes producing actin branches [33]. These findings

suggest that different Arp2/3 iso-complexes engage fundamentally distinct mechanisms depending on whether activation drives linear filament formation or actin branching. Our structure study using recombinant Arp2/3 complex showed the SPIN90 can generate linear actin filaments with ArpC1B and ArpC5L containing Arp2/3 [35]. However, the structure of the SPIN90–Arp2/3 complex, which contains Arp2/3 complex purified from a natural bovine source, does not have sufficient side-chain resolution to determine isoform-specific information [12,36]. Hence, it is not known if ArpC1A and/or ArpC5 containing complex can also generate linear filaments.

In this study, using in vitro biochemical approaches, we found that only the ArpC5L-containing Arp2/3 complex can generate linear actin filaments. Moreover, SPIN90 accumulates at the leading edge of lamellipodia, where it recruits and activates ArpC5L-, but not ArpC5-containing Arp2/3 complexes. These linear filaments nucleated by SPIN90-Arp2/3-ArpC5L complexes shape the architecture of lamellipodial actin, impacting actin dynamics and leading-edge protrusion.

Results

Spin90 preferentially activates ArpC5L-containing Arp2/3 complexes

Using purified recombinant human Arp2/3 iso-complexes with defined compositions, we performed pyrene actin polymerisation assays to examine their capacity to accelerate actin polymerisation when activated by SPIN90. We found that, in the presence of SPIN90, Arp2/3 complexes containing ArpC1A-ArpC5L or ArpC1B-ArpC5L significantly increase the rate of actin polymerization compared to controls lacking SPIN90 (Fig. 1A). In contrast, Arp2/3 complexes containing ArpC1A-ArpC5 or ArpC1B-ArpC5 only induced actin polymerisation at levels slightly above controls when activated by SPIN90. These differences suggest SPIN90 only efficiently activates Arp2/3 complexes containing ArpC5L to generate linear filaments.

To further confirm this, we performed TIRF microscopy to directly observe the generation of linear actin filaments by the different Arp2/3 iso-complexes in the presence of SPIN90. Actin alone, or in combination with Arp2/3 complexes, does not efficiently nucleate filament formation (Fig. 1B). When incubated with SPIN90, Arp2/3 complexes containing ArpC5, whether paired with ArpC1A or ArpC1B, had an extremely limited increase in actin nucleation. In contrast, Arp2/3 complexes containing ArpC5L, regardless of the ArpC1 isoform, produce linear filaments with 20- to 40-fold greater efficiency in the presence of SPIN90 (Fig. 1B). These results clearly show that linear actin filaments are generated by SPIN90-activated ArpC5L-containing Arp2/3 complexes.

SPIN90 has a higher affinity for Arp2/3 complexes containing ArpC5L

Our finding that only ArpC5L-containing complexes can be efficiently activated by SPIN90 raises the question: what is the molecular basis for the differing efficiencies in linear filament nucleation among Arp2/3 iso-complexes? The recent structure of SPIN90

112 in complex with Arp2/3 reveals it binds directly to the ArpC5/ArpC5L subunit, as well as
113 to Arp2, Arp3, ArpC2 and ArpC4 (Fig. 2A, S1A) [12,37,38]. Nevertheless, the resolution of
114 current available structure is insufficient to resolve the side chain and N-terminus of
115 ArpC5 subunit [12,36]. Consequently, it remains unclear whether ArpC5 or ArpC5L is present
116 in the bovine Arp2/3 complex interacting with SPIN90 (Fig. 2B). In contrast and consistent
117 with our biochemical observations, in the structure of SPIN90-with defined recombinant
118 human Arp2/3 complex, it interacts with ArpC5L [35].

119 Given our observations, we wondered whether the ArpC5 subunit incorporation
120 determines the affinity between SPIN90 and the Arp2/3 complex. We tried several
121 approaches to examine the affinity between Arp2/3 iso-complexes and SPIN90. However,
122 surface plasmon resonance, microscale thermophoresis and isothermal titration
123 calorimetry failed to yield reproducible results. Finally, we examined the binding
124 between Arp2/3 iso-complexes and SPIN90 using GST pull-down assays. We found that
125 GST-SPIN90 pulled down more Arp2/3 complexes containing ArpC5L compared to those
126 with ArpC5, regardless of the ArpC1 subunit isoform (Fig. S1B).

127 To quantify the affinity of SPIN90 for Arp2/3 complexes containing either ArpC5L or ArpC5,
128 we performed GST pull-down assays on Arp2/3 complexes containing ArpC1B/ArpC5 or
129 ArpC1B/ArpC5L (Fig. 2C, D). We found both ArpC5 (K_{off} = 0.067 min^{-1}) or ArpC5L (K_{off} =
130 0.045 min^{-1}) containing complex exhibit similar dissociation rate with SPIN90 (Fig. 2C).
131 As the dissociation is very slow (half-time > 10 min), it is negligible during binding analysis
132 (Fig. 2D). Recent work has shown that SPIN90 forms a homodimer that simultaneously
133 binds two Arp2/3 complexes [37,38]. Thus, we used the Hill equation to fit the experimental
134 data and examine whether the Arp2/3 complex binds to SPIN90 in a cooperative manner
135 (Fig. 2D, S1C). The fitting revealed that SPIN90 binds the ArpC1B/ArpC5L-containing
136 Arp2/3 complex with a dissociation constant (K_D) of 3.01 ± 0.85 μM and a Hill coefficient
137 of 1.59 ± 0.67, suggesting the possible presence of positive cooperativity. In contrast, the
138 low amount of ArpC5-containing complex pulled down with GST-SPIN90 prevented
139 reliable fitting so a dissociation constant (K_D) could not be determined. These results
140 confirmed that the ArpC5 subunit isoforms have a strong impact on the affinity of SPIN90
141 for Arp2/3 iso-complexes. Furthermore, it provides an explanation why, SPIN90
142 effectively only activates ArpC5L-containing Arp2/3 complexes to generate linear actin
143 filaments in our in vitro experiments.

144 **SPIN90 is enriched at the leading edge**

145 Another key question is the physiological impact of the selective interaction between
146 SPIN90 and Arp2/3–ArpC5L in cells. To study the impact of SPIN90 and Arp2/3 on the
147 cellular actin, we used B16 cells which have large and constant lamellipodial branched
148 actin networks [39,40]. We began by assessing the expression level of ArpC5 and ArpC5L
149 containing Arp2/3 complexes in B16 cells through quantitative immunoblot analysis,
150 using recombinant mouse ArpC5 and ArpC5L subunits as standards (Fig. 3A). We found

151 that ArpC5 and ArpC5L are both expressed in B16 cells, with ArpC5L levels being ~1.7-
152 fold higher than ArpC5.

153 Then, we investigated the localisation of SPIN90 in B16 cells. We tested several SPIN90
154 antibodies, including commercial and homemade ones, but none worked on mouse cell
155 lines for immunofluorescence analysis. We therefore expressed Ruby-tagged SPIN90 to
156 visualize the localization of SPIN90 in live cells. We found that Ruby-SPIN90 is
157 predominantly cytoplasmic, but the protein is enriched at the leading edge of
158 lamellipodia which is not observed with the GFP internal control (Fig. 3B, Movie S1). A
159 similar accumulation at the leading edge was observed for a Ruby-SPIN90 Nter construct
160 that lacks the Arp2/3 interacting C-terminal Leucine Rich Region (LRR) of SPIN90 (Fig. 3B,
161 Movie S2). This localisation demonstrates that the N-terminus of SPIN90 responds to an
162 upstream signal responsible for determining the localisation of SPIN90.

163 **Both SPIN90 and Arp2/3 integrate into lamellipodial actin**

164 To visualize both ArpC5L and SPIN90 at the same time we expressed Ruby-SPIN90 in B16
165 cell lines in which NeonGreen is linked to the N-terminus of ArpC5L at its endogenous
166 gene locus (Fig. S2A). We cannot distinguish ArpC5L bound to SPIN90 from ArpC5L
167 located at actin branches, but we observed that both ArpC5L and SPIN90 accumulate at
168 the leading edge of lamellipodia (Fig. 4A, B, Movie S3). Interestingly, during live imaging,
169 we observed that both proteins initially appear at the leading edge and then move
170 rearward toward the cell body before disappearing (Movie S3). Hence, the trajectories of
171 NeonGreen-ArpC5L and Ruby-SPIN90-FL display similar patterns, characterized by
172 straight lines perpendicular to the leading edge (Fig. 4A). This is the first time such
173 retrograde flow of SPIN90 has been seen in lamellipodia (Fig. 4A), although the rearward
174 flow of Arp2/3 complexes has been described [39]. Indeed, as a part of the Arp2/3 complex,
175 ArpC5L integrates into branched actin networks with or without SPIN90, as does ArpC5.

176 To determine whether SPIN90 integrates into the actin network through its interaction
177 with Arp2/3 complexes, we examined the behaviour of Ruby-SPIN90 Nter in B16 cells
178 expressing endogenous NeonGreen-ArpC5L. Live cell imaging reveals that while
179 NeonGreen-ArpC5L undergoes retrograde flow, Ruby-SPIN90 Nter remained at the
180 leading edge and did not move inward toward the cell body (Movie S4). The trajectories of
181 NeonGreen-ArpC5L and Ruby-SPIN90 Nter exhibit distinct patterns (Fig. 4A).

182 To analyse the movement of SPIN90 and ArpC5L in more detail, we generated
183 kymographs, which revealed that both proteins move at similar velocities (Fig. 4B). In
184 contrast, SPIN90-Nter does not show directional movement, so kymographs cannot be
185 used to analyse its velocity.

186 Taken together, our observations indicate that SPIN90, through its binding to Arp2/3
187 complexes, integrates into lamellipodial networks and undergoes retrograde flow.

188 **SPIN90 enhances recruitment of ArpC5L but not ArpC5 to the leading edge**

189 Our in vitro data demonstrate that SPIN90 interacts much better with Arp2/3 complexes
190 containing ArpC5L, than those with ArpC5. To examine if SPIN90 enhances the
191 recruitment of ArpC5L-containing Arp2/3 complexes, we quantified the relative level of
192 NeonGreen-ArpC5L at the leading edge in the presence and absence of SPIN90 (Fig. 5A).
193 We observed that in SPIN90 depleted cells (Fig. S2), the relative level of NeonGreen-
194 ArpC5L signal at the leading edge is reduced compared to control cells. When ArpC5 is
195 knocked down, we observed increased recruitment of NeonGreen-ArpC5L to the leading
196 edge, to compensate for the absence of ArpC5-containing complexes. Importantly, the
197 depletion of SPIN90 in the absence of ArpC5 still results in reduced recruitment of
198 ArpC5L to the leading edge (Fig. 5A). Meanwhile, our Western blots confirmed that
199 SPIN90 depletion does not affect the expression of ArpC5 isoforms, in addition the
200 depletion of ArpC5 or ArpC5L has little impact on the expression of the other isoform (Fig.
201 S2). In contrast to ArpC5L, the relative signal of endogenous NeonGreen tagged ArpC5 at
202 the leading edge does not negatively correlate with the depletion of SPIN90 as it
203 increases (Fig. 5B). To rule out the possibility that our observation was due to the side
204 effect of the NeonGreen tag on the ArpC5 subunit, we performed immunofluorescence
205 on siRNA-treated B16 cells. As expected, depletion of ArpC5 led to a decrease in the
206 ArpC5/ArpC2 ratio. We observed that the ArpC5/ArpC2 ratio increased in both ArpC5L-
207 and SPIN90-depleted cells (Fig. S2C). Our observations support the hypothesis that
208 SPIN90 enhances the recruitment of ArpC5L, but not ArpC5, to the leading edge.

209 **SPIN90 regulates lamellipodial actin architecture via ArpC5L**

210 Arp2/3-mediated branches are geometrically constrained to form at an angle of
211 approximately 70 degrees [7]. However, it has been reported that Arp2/3 complexes
212 containing either ArpC5 or ArpC5L have a distinct impact on the architecture of
213 lamellipodial actin networks although the mechanistic basis for this difference has not
214 been established [25]. Given that SPIN90 generates linear filaments only with ArpC5L-
215 containing complexes, we wondered what impact its presence has on the architecture of
216 lamellipodial actin networks.

217 By exploiting the sensitivity of polarized light excitation to the orientation of fluorophores
218 attached to the actin filaments, polarized fluorescence microscopy is a unique approach
219 to measure actin filament organization [41]. It allows the acquisition and processing of large
220 amounts of cellular data quickly compared with other methods, such as cryo-electron
221 microscopy. Using this approach, we quantified the organization of actin filaments in
222 lamellipodia, excluding microspikes, in Alexa-488 phalloidin-stained cells. The Alexa-488
223 conjugate in phalloidin is constrained in mobility and is parallel to the axis of the actin
224 filament helix [41]. Thus, the orientation of Alexa-488 is a direct readout of actin filament
225 mean orientation (angle rho, ρ) within a scale of ~200nm (i.e. the optical resolution limit,
226 Fig. 6A, B). Its angular spread around the mean orientation at each pixel is a

227 complementary readout of actin filament alignment (angle psi, ψ) at the molecular level,
228 within the scale of ~200 nm (Fig. 6A, S3A-C).

229 We measured high ψ values for lamellipodial actin (mean = 157°) in wildtype cells, as well
230 as in all KO cell lines (Fig. S3A-C), with no detectable statistical difference among the
231 different cell lines. This finding is in line with electron microscopy showing that
232 lamellipodial actin filaments explore varying orientations within the scale of ~200 nm (Fig.
233 6A, B), and with quantification of branch densities which were comparable in tomograms
234 of WT, ArpC5 KO and ArpC5L KO cell lines [25].

235 Importantly, quantification of mean actin filament orientations showed distinct
236 differences among the different cell lines (Fig. 6A-F and Fig. S3D). Whereas lamellipodial
237 actin in WT cells enriches in populations more perpendicular to the leading edge, the
238 distribution of filament orientations, both per pixel (Fig. 6C, D and Fig. S3D) and averaged
239 per lamellipodium (Fig. 6E, F), is much broader in ArpC5 KO cells. This increased
240 variability, reflected by the higher standard deviation (SD) of the respective distribution,
241 indicates the coexistence of filament populations more parallel to the leading edge.
242 Importantly, lamellipodial actin filaments in both ArpC5L KO and SPIN90 KO cells not
243 only remained enriched in populations more perpendicular to the leading edge, but the
244 respective distributions, both per pixel (Fig. 6B-D and Fig. S3D) and averaged per
245 lamellipodium (Fig. 6E, F), were also narrower than in WT cells. This reflects the presence
246 of a larger population of filaments with angles perpendicular to the leading edge. Our
247 observations are fully consistent with the quantification of filament angles from cryo-
248 electron tomograms in ArpC5L KO cells [25], and importantly further demonstrate that
249 SPIN90 regulates lamellipodial actin architecture via ArpC5L.

250 Arp2/3-mediated branches follow a characteristic average 70-degree geometry whereas
251 SPIN90–Arp2/3-nucleated linear actin filaments can in principle orient in all directions.
252 We therefore hypothesized that the absence of this linear filament population is
253 responsible for the enrichment of filaments with angles perpendicular to the leading
254 edge in both ArpC5L KO and SPIN90 KO cells. Moreover, this predicts a broader
255 distribution of filament angles in cells overexpressing SPIN90. Consistent with this, we
256 found that cells expressing Ruby-SPIN90 had a wider distribution of filament angles than
257 those expressing Ruby-SPIN90 Nter which cannot interact with the Arp2/3 complex, the
258 latter being comparable to wildtype cells (Fig. 6G, H and Fig. S3E, F).

259 **SPIN90 regulates lamellipodial protrusion**

260 To examine the impact of the SPIN90 interaction with ArpC5L-containing Arp2/3
261 complexes on lamellipodial protrusion, we generated B16 cells with endogenously
262 tagged GFP-β-actin and lacking either the ArpC5 isoforms or SPIN90 respectively (Fig. 7A,
263 S4A). As previously reported by Fässler et al. (2023), we observed that in B16 cells the
264 absence of ArpC5 reduces lamellipodial width, while the loss of ArpC5L increases it (Fig.
265 7B). In contrast the SPIN90 KO cells have lamellipodia of similar width to those of wild-

266 type cells (Fig. 7B). Quantification of the lamellipodial actin density (GFP-β-actin
267 intensity), however, revealed that the actin density increased in SPIN90 KO cells
268 compared to wild type controls. A similar increase in, lamellipodial actin density was also
269 observed in the ArpC5L KO cells (Fig. 7B). In contrast, loss of ArpC5 resulted in reduce
270 actin density.

271 We performed FRAP analysis and quantified the protrusion rate and rearward flow of
272 lamellipodial actin (Fig. 7C, D). Our results revealed that the loss of ArpC5 reduces the
273 lamellipodial protrusion rate, while the absence of ArpC5L does not have a strong impact
274 on protrusion. Nevertheless, we found that SPIN90 KO cells consistently exhibit a slower
275 protrusion rate compared to controls (Fig. 7D). We did not observe any significant
276 difference in rearward flow between the wild-type and the three KO cell lines. The sum of
277 rearward flow and protrusion rate was considered the lamellipodial actin polymerization
278 rate (Fig. S4B). When we calculated protrusion efficiency by dividing the protrusion rate
279 by the actin polymerization rate, we found that ArpC5L KO cells maintain a protrusion
280 efficiency comparable to wildtype cells, whereas both ArpC5 KO and SPIN90 KO cells
281 have reduced protrusion efficiency (Fig. 7D). Consistent with this, in a random migration
282 assay using unlabelled B16 cells, we observed that ArpC5 KO and SPIN90 KO cells
283 migrated more slowly compared with wild-type and ArpC5L KO cells (Fig. 7E).

284 We hypothesized that SPIN90–Arp2/3–nucleated linear actin filaments help support
285 lamellipodial protrusion. To test this notion, we overexpressed Ruby-SPIN90 in B16 cells
286 and found as predicted that Ruby-SPIN90 increased the lamellipodial protrusion rate (Fig.
287 7F).

288 **Discussion**

289 Using in vitro biochemical approaches, we have now shown that the initiation of linear
290 actin filaments by Arp2/3 complexes is determined by the composition of their ArpC5
291 subunits. Only Arp2/3 complexes containing ArpC5L and not those with ArpC5, can be
292 efficiently activated by SPIN90 (Fig. 1, 8A), due to their differing affinity for this nucleation
293 promoting factor (Fig. 2). This makes SPIN90 the first Arp2/3 activator with a clear
294 preference for a defined subset of Arp2/3 iso-complexes. Our findings strengthen the
295 hypothesis that Arp2/3 iso-complexes have distinct molecular and cellular properties
296 determined by their subunit composition.

297 We also found that SPIN90 is enriched at the leading edge of lamellipodia (Fig. 3B) where
298 it enhances the recruitment of ArpC5L- but not ArpC5-containing Arp2/3 iso-complexes
299 (Fig. 5, 8A). Importantly, we observed the rearward flow of SPIN90 (Fig. 4). Retrograde
300 lamellipodial actin flow is known to result from myosin contraction and the resistive
301 forces encountered during protrusion [42,43]. It is also established that after initiating a
302 branch, the Arp2/3 complex remains at the branching point and becomes integrated into
303 the branched actin network [39]. The fact that SPIN90, but not its N-terminal domain which
304 cannot bind Arp2/3, undergoes rearward flow indicates that SPIN90 and ArpC5L

containing Arp2/3 integrate into lamellipodial actin together, presumably through crosslinking between SPIN90-Arp2/3-nucleated linear filaments and the rest of the lamellipodial actin.

Furthermore, using polarized fluorescence microscopy [41], we found that both SPIN90 and ArpC5L contribute to the enrichment of actin filaments with angles more parallel to the leading edge, whereas those formed by ArpC5 are more perpendicular (Fig. 6A-F). This is likely because branches generated by Arp2/3 are constrained by two factors: the orientation of pre-existing mother filaments and the fixed 70° branching angle dictated by the Arp2/3 complex structure. In contrast, linear filaments generated by SPIN90–Arp2/3–ArpC5L are likely freer to orient in any direction before being crosslinked to actin filaments in the lamellipodia (Fig. 8). The presence of SPIN90 and ArpC5L-containing complexes therefore increases the diversity of filament orientations at the leading edge.

Our observations of ArpC5 KO and ArpC5L KO lamellipodial actin networks using polarized fluorescence microscopy are fully consistent with previous reports based on high-resolution electron microscopy [25]. Importantly, they further demonstrate that SPIN90 works together with ArpC5L to regulate lamellipodial actin architecture. Although, compared with EM, we lack information on the orientation of individual actin filaments, our approach provides accurate measurements of the mean orientation and alignment of actin filaments at the molecular scale across a large number of cells, as well as in much larger areas. This approach also offers the possibility of studying actin architecture through live imaging [41], thereby enabling simultaneous observation of cell behaviour and actin organization in the future.

Finally, we show that depletion of SPIN90 downregulates both the lamellipodial protrusion rate and the speed of cell motility (Fig. 7D, E). We believe that actin dynamics and architecture — including both filament orientation angles and their distribution — must be finely tuned to ensure efficient lamellipodial protrusion and cell migration. Accordingly, SPIN90 KO cells, which exhibit a narrower distribution of filament orientations, display reduced protrusion efficiency. In contrast, despite having a similar lamellipodial architecture, ArpC5L KO cells maintain a protrusion rate comparable to that of wild-type cells. This may be attributed to the positive correlation between ArpC5-nucleated branches and Ena/VASP activity, which promotes rapid actin filament elongation [25]. Moreover, the low protrusion speed and motility observed in ArpC5 KO cells are likely the result of a combination of their negative correlation with Ena/VASP and an actin architecture, in which too many filaments are oriented toward the leading edge at shallow angles. Here we illustrate the importance of actin architecture on the lamellipodia protrusion efficiency. Nevertheless, a systematic understanding of how actin architecture and dynamics impact protrusion efficiency, particularly under different mechanical external conditions remains to be established.

Acknowledgements

This project has received funding from the European Research Council (ERC) under the European Union's Horizon 2020 research and innovation programme (grant agreement No 810207 to M.W.). L.C. was supported by the European Union's Horizon 2020 Marie Sklodowka-Curie individual fellowship program (H2020-MSCA-IF-101028239 – MolecularArp). A.J. was supported by the Fondation Bettencourt-Schueller (Impulscience program). G. R.-L. was supported by the Fondation pour la Recherche Medicale (grant EQU202203014630). MW is supported by the Francis Crick Institute, which receives its core funding from Cancer Research UK (CC2096), the UK Medical Research Council (CC2096), and the Wellcome Trust (CC2096). M.V. and S.B. are supported by funding from the French National Research Agency (ANR) grant Equipex+ IDEC (France 2030 investment plan ANR-21-ESRE-0002) and the France-BioImaging infrastructure (ANR-10-INBS-04). We thank Tianyang Liu (Birkbeck College, UK) for comparing the published electron density map with different structural models. We thank Jean-Jacques Honorine (Institut Fresnel, France) for technical help with the calibration of the polarized fluorescence microscope. We acknowledge the Photonics facility of the Institut Fresnel. We thank Jeremy Carlton (King's College London, UK) and Klemens Rottner (Helmholtz Centre for Infection Research, Germany) for feedback on the manuscript. For the purpose of Open Access, the authors have applied a CC BY public copyright licence to any Author Accepted Manuscript version arising from this submission.

Competing interest statement

The authors declare that they have no competing interests.

367 **Figure Legends**

368 **Figure 1. SPIN90 selectively activates ArpC5L containing Arp2/3 complexes**

369 (A) SPIN90 efficiently activates ArpC5L but not ArpC5 containing Arp2/3 complexes.
370 Representative plots of pyrene-actin polymerization assays with 10 nM Arp2/3
371 complex, 100 nM SPIN90 and 2.5 μM actin (5 % pyrene labelled). It demonstrates
372 that ArpC5L- but not ArpC5-containing Arp2/3 complexes activated by SPIN90
373 induce rapid actin polymerization, regardless of the ArpC1 isoform. The
374 experiments were repeated independently three times and yielded similar
375 results.
376 (B) Representative TIRF images demonstrate that ArpC5L- but not ArpC5-containing
377 complex activated by SPIN90 efficiently generate actin filaments. A mixture of 20
378 nM Arp2/3 complex, 200 nM SPIN90 and 0.5 μM actin (15 % Alexa 488 labelled)
379 was observed overtime. The graph shows quantitative analysis of filament
380 density over time from three independent technical replicates. The points
381 indicate the mean density, and the error bars represent the standard deviation.

382 **Figure 2. SPIN90 has a higher affinity for Arp2/3 complexes with ArpC5L than ArpC5**

383 (A) Surface representation of the Arp2/3 complex from the SPIN90-Arp2/3 complex
384 structure (PDB: 6DEC). Residues in Arp2/3 complex subunits contacting the two
385 SPIN90 molecules are shown in darker colours.
386 (B) The 2Fo-Fc electron density map of Arp2/3 crystal structure in complex with
387 SPIN90 (purple) is shown at a contour level of 1.5σ (blue mesh). ArpC5L (dark
388 yellow) is superimposed with ArpC5 (light yellow) subunit determined in the
389 structure. The remaining subunits of Arp2/3 complex are coloured in grey.
390 (C) Immunoblots using an ArpC2 antibody show the amount of Arp2/3 complex
391 attached to SPIN90 different time points after free Arp2/3 complexes were
392 washed out. The graph shows the quantification of average normalised ArpC2
393 from three independent replicates. The data was fit with single exponential
394 equation.
395 (D) Immunoblots using an ArpC2 antibody show the amount of Arp2/3 complex
396 containing ArpC1B pulled down with GST–SPIN90-Cter. Both blots were run on
397 the same gel and developed on the same membrane to allow a direct
398 comparison of signal intensity. The graph shows the quantification of average
399 normalized ArpC2 intensity from three independent replicates. The data was fit
400 with Hill equation.

401 **Figure 3. SPIN90 localizes at the leading edge and integrates into lamellipodial**
402 **actin networks.**

403 (A) Quantitative immunoblot analysis of endogenous levels of ArpC5 isoforms in
404 B16 cells using recombinant His-tagged ArpC5 and His-tagged ArpC5L as

standards. The average concentrations and standard deviations from three independent replicates are shown in the table on the right.

(B) Schematic shows the two Ruby-tagged SPIN90 constructs expressed in cells. Representative live images show B16 cells overexpressing GFP (volume marker) together with Ruby–SPIN90 (upper) or with Ruby-SPIN90 Nter (lower). Signal intensity (right) is quantified by normalizing the intensity at the leading edge (solid line) compared to that 2 μm from the leading edge (dashed line). Each pair of points represents measurements from the same cell with the different colours representing data from three independent replicates. A two-tailed paired t-test is used to estimate the p-value.

Figure 4. SPIN90 integrates into the lamellipodia with Arp2/3 complex

(A) Representative maximum intensity projection over 14 seconds for cells expressing endogenous NeonGreen–ArpC5L, together with overexpressed Ruby–SPIN90 or Ruby–SPIN90-Nter. ArpC5L and Ruby–SPIN90, but not Ruby–SPIN90-Nter undergo rearward movement in the lamellipodium (highlighted with yellow arrows). The similar trajectory pattern observed in all the cells (20 for SPIN90-FL and 13 for SPIN90-Nter) across three independent replicates.

(B) Representative live image (upper) of B16 cells with endogenously labelled NeonGreen-ArpC5L and overexpressing Ruby–SPIN90. Kymographs (lower), generated from the orange lines in the upper images, show that ArpC5L (left) and SPIN90 (right) exhibit directional movement, highlighted with blue arrows. Quantitative analysis (right panel) of the rearward flow of ArpC5L and SPIN90 respectively. Different colours indicate results from three independent replicates. A two-tailed unpaired t-test with Welsh's correction is used to estimate the p-value.

Figure 5. SPIN90 enhances the recruitment of ArpC5L but not ArpC5 to the leading edge

Representative images of live cells expressing endogenous NeonGreen–ArpC5L (A) or ArpC5-NeonGreen (B) after treatment with the indicated siRNAs. Allstar represents siRNA control. The graphs show quantification of the ArpC5L or ArpC5 signal intensity at the leading edge normalised with the expression level of NeonGreen tagged protein in the different conditions. Each point represents an individual cell, with different colours indicating 3 independent experimental replicates. For each repeat, 8-15 cells were imaged and quantified. The mean of each experiment is shown as a circle, and error bars are standard deviation. A two-tailed unpaired t-test was used to calculate the p-value.

Figure 6. The organisation of actin filaments at the leading edge of B16 cells.

(A) Schematic representation of ρ (rho) and ψ (psi) in the organization of the actin network.

(B) Representative images of an Alexa-488 phalloidin stained B16 cell for each cell line as indicated. The coloured region in the lamellipodium is the result of polarimetry analysis within a 0.65 μm (10-pixel) region from the leading edge to determine the mean actin filament orientation in each pixel. The mean filament orientation per pixel is represented with a stick whose orientation corresponds to filament orientation (angle rho, ρ) and whose color depicts filament orientation with respect to the leading edge (angle rho_c, ρ_c) within the 0–180° range according to the colour bar. The stick maps of a representative ROI (labelled with white rectangles) are zoomed in and shown.

(C) The polar histogram shows the statistical distribution of actin filament angles (ρ_c) per pixel within the 0–90° range relative to the leading edge of all the cells, with 38 to 55 cells analysed per condition across three independent repeats. The average $< \rho_c >$ and standard deviation for each cell line are indicated. The colours correspond to the colour bar shown in panel A.

(D) Violin plot showing the statistical distribution of actin filament angles (ρ_c) per pixel within the 0–90° range, as shown in panel B. A two-tailed Mann–Whitney test was used to calculate the p-value between individual cells under two conditions. The medians and interquartile ranges are shown as black lines, while the means and standard deviations are shown as blue dots with error bars.

(E) The statistical results of the average lamellipodial actin filament angle $< \rho_c >$ relative to the leading edge within the 0–90° range in individual wildtype, ArpC5, ArpC5Lor SPIN90 knockout cells. Each point represents the mean angle of actin filaments relative to the leading edge in a single cell from three independent experiments, the latter shown in different colours. Mean ± SD for each experimental condition is indicated. A two-tailed Welch's t-test is used to estimate the p-value between the means under two conditions.

(F) The statistical results of the standard deviation (SD) of actin filament angles relative to the leading edge within the 0–90° range in individual wildtype, ArpC5, ArpC5L, or SPIN90 knockout cells. Each point represents the SD of actin filaments relative to the leading edge in a single cell from three independent experiments, the latter shown in different colours. Mean ± SD for each experimental condition is indicated. A two-tailed Mann Whitney test is used to estimate the p-value between individual cells under two conditions.

(G) Representative images of Alexa-488 phalloidin stained B16 cell (right) overexpressing Ruby-SPIN90 (left). The zoomed-in image shows the mean actin filament orientation per pixel within the ROI (white rectangle) as in panel A.

(H) The polar histogram shows the statistical distribution of actin filament angles (ρ_c) per pixel within the 0–90° range relative to the leading edge in all cells overexpressing either Ruby-SPIN90 (61 cells) or Ruby-SPIN90 Nter (59 cells),

483 across three independent experimental repeats. The average < ρ_c > and standard
484 deviation for each experimental condition are indicated. The colours correspond
485 to the colour bar shown in panel A.

486 **Figure 7. SPIN90 impacts the lamellipodia protrusion and cell motility.**

487 (A) Representative image stills of WT, ArpC5, ArpC5Land SPIN90 knockout B16 cells
488 expressing endogenously tagged GFP β-actin.
489 (B) The quantification of lamellipodia width, lamellipodial actin density. Each point
490 represents an individual cell, with different colours indicating independent
491 experimental replicates. The mean of each experiment is shown as a circle, and
492 error bars are standard deviation. A two-tailed paired t-test was used to
493 estimate the p-value between the means under two conditions.
494 (C) Representative image still (upper) from a FRAP assay on a B16 cell with
495 endogenously GFP tagged β–actin. The kymograph (lower) shows the cell
496 protrusion (indicated by straight line) and rearward flow (indicated by dashed
497 line), made visible by the FRAP region.
498 (D) The quantification of lamellipodial protrusion rate, rearward flow and protrusion
499 efficiency. Each point represents an individual cell, with different colours
500 indicating independent experimental replicates. The mean of each experiment is
501 shown as a circle, and error bars are standard deviation. A two-tailed paired t-
502 test was used to estimate the p-value between the means under two conditions.
503 (E) Quantification of B16 cell random migration speed. Each point represents an
504 individual cell, with different colours indicating 3 or 4 independent replicates.
505 The mean of each experiment is shown as a circle, and error bars represent
506 standard deviation. A two-tailed unpaired t-test was used to estimate the p-
507 value between the means under two conditions.
508 (F) Representative images (left panels) of the leading edge of B16 cells
509 overexpressing either Ruby, or Ruby-SPIN90. The right panel shows the
510 protrusion rate of these cells. Each point represents an individual cell, with
511 different colours indicating independent experimental replicates. The mean of
512 each experiment is shown as a circle, and error bars are standard deviation. A
513 two-tailed paired t-test was used to estimate the p-value between the means
514 under two conditions.

515 **Figure 8. Schematic summary**

516 (A) In migrating cells, SPIN90 recruits the ArpC5L-, but not the ArpC5-containing
517 complex, to the lamellipodial leading edge (1). Meanwhile, both ArpC5L- and
518 ArpC5-containing complexes generate branches at the lamellipodia (2). Thus,
519 SPIN90 and Arp2/3 iso-complexes integrate into the lamellipodial actin network,
520 contributing to the formation of a complex actin architecture that ensures
521 efficient protrusion (3).

522 (B) ArpC5 KO cells (left panel), the ArpC5L-containing complex participates in the
523 formation of both linear and branched actin filaments. Consequently, the
524 distribution of filament orientations in their lamellipodia is much fig than that of
525 the wild type. In contrast, in ArpC5L KO cells (right panel), the ArpC5-containing
526 complex generates only branched actin filaments, resulting in a narrower
527 distribution of filament orientations.

528 **Supplementary Figure legends**

529 **SF 1. Binding between the Arp2/3 complex and SPIN90.**

530 (A) Sequence alignment between ArpC5 and ArpC5L subunit. The interface binding
531 SPIN90 is highlighted with colours: residues that are identical in both isoforms
532 are shown in yellow, while distinct residues are shown in cyan.
533 (B) Immunoblot using an ArpC2 antibody demonstrate that ArpC5L-containing
534 Arp2/3 complexes interact more strongly with GST–SPIN90-Cter than those with
535 ArpC5.
536 (C) The immunoblot showing the results in Fig. 2C were developed on the same blot.

537 **SF 2. The western blot of siRNA treated cells.**

538 (A) The western blot of siRNA treated ArpC5-NeonGreen B16 cells.
539 (B) The western blot of siRNA treated NeonGreen-ArpC5L B16 cells.
540 (C) Representative immunofluorescence images of siRNA-treated B16 cells. For
541 each repeat, the ratio of ArpC5 to ArpC2 signal is normalized to the AllStar
542 control. Quantitative results are shown in the right panel. Each dot represents an
543 individual cell, and the circles indicate the mean of each repeat. The Wilcoxon
544 test was used to examine statistical significance.

545 **SF 3. The organisation of lamellipodial actin.**

546 (A) Corresponding to Fig 6A, B. Representative images of an Alexa-488 phalloidin
547 stained B16 cell for each cell line as indicated. The mean filament orientation
548 per pixel is represented with a stick whose orientation corresponds to filament
549 orientation (angle rho, ρ) and whose colour depicts filament alignment (angle
550 psi, ψ) according to the colour bar. The stick maps of a representative ROI
551 (labelled with white rectangles) are zoomed in and shown.
552 (B) The histogram shows the statistical distribution of filament alignment angles ψ
553 per pixel of all the individual cells, with 38 to 55 cells analysed per condition
554 across three independent repeats. The average <ψ> and SD for each cell line are
555 indicated. The colours correspond to the colour bar shown in panel A.
556 (C) Statistical analysis of the average <ψ> in each individual wildtype, ArpC5, and
557 ArpC5L or SPIN90 knockout cells. Mean ± SD for each cell line is indicated. A
558 two-tailed Welch's t-test is used to estimate the p-value between individual cells
559 under two conditions.

(D) Corresponding to Fig 6C. The polar histogram shows the statistical distribution of actin filament angles (ρ_c) per pixel within the 0–180° range relative to the leading edge in all cells. The average ρ_c per pixel and SD for each cell line are indicated. The colours correspond to the color bar shown in panel Fig 6A.

(E) Corresponding to Fig. 6H. The polar histogram shows the statistical distribution of actin filament angles (ρ_c) per pixel within the 0–180° range relative to the leading edge in all cells, overexpressing either Ruby-SPIN90 or Ruby-SPIN90 Nter. The average $< \rho_c >$ and standard deviation for each experimental condition are indicated.

(F) The statistical results of the average lamellipodial actin filament angle relative to the leading edge within the 0–90° range in individual wildtype cells (also shown in Fig. 6H) or cells overexpressing either Ruby-SPIN90 or Ruby-SPIN90 Nter. Each point represents the mean angle of actin filaments relative to the leading edge in a single cell from three independent experiments, the latter shown in different colours. Mean ± SD for each experimental condition is indicated. A two-tailed Welch's t-test is used to estimate the p-value between the means under two conditions.

SF 4. Analysis of KO cell lines.

(A) The left panel shows the absence of targeted gene, while the right panel show the endogenous labelling of GFP-β-actin in these cell lines.

(B) The graphs show quantification of the polymerization rate which is calculated by summing the rearward flow and protrusion rates. Each point represents an individual cell, with different colours indicating independent experimental replicates. The mean of each experiment is shown as a circle, and error bars indicated the standard deviation. A two-tailed paired t-test was used to calculate the p-value between the means under two conditions.

Movies

Movie 1. Movie showing live imaging of B16 cells overexpressing GFP (a volume marker) and Ruby-SPIN90, corresponding to Fig. 3B (middle panel). The right panel shows inverted-intensity live images of each channel.

Movie 2. Movie showing live imaging of B16 cells overexpressing GFP (a volume marker) and Ruby-SPIN90 Nter, corresponding to Fig. 3B (lower panel). The right panel shows inverted-intensity live images of each channel.

Movie 3. Movie showing live imaging of NeonGreen-ArpC5L B16 cells overexpressing Ruby-SPIN90, corresponding to Fig. 4A (upper panel). The middle and the right panel show inverted-intensity live images of each channel.

596 **Movie 4**. Movie showing live imaging of NeonGreen-ArpC5L B16 cells overexpressing
597 Ruby-SPIN90, corresponding to Fig. 4A (lower panel). The middle and the right panel
598 show inverted-intensity live images of each channel.

599

Materials and Methods

Protein purification and preparation

Recombinant human Arp2/3 iso-complexes with defined composition (Uniprot P61160, P61158, Q92747, O15143, O15144, O15145, P59998, Q9H9F9 and Q98PX5) were purified as previously reported [44]. In this study, we focus on the Arp2/3 complex with Arp3 background because our previous study showed that both Arp3B and Arp3 containing Arp2/3 complex can generate linear filaments with SPIN90 [33]. Skeletal muscle α-actin was purified from rabbit muscle following the published protocol [45]. GST-tagged and untagged human SPIN90 C-terminus (267-715, UniProt Q9NZQ3-3) were purified as previously reported [46]. Similarly, GST-tagged and untagged mouse SPIN90 full length (UniProt Q9ESJ4) were purified. Actin was fluorescently labelled on its lysine 328, with Alexa-488 succinimidyl ester (Life Technology) following the reported protocol [47]. Actin was labelled with N(1-pyrene)-iodoacetamide (Thermo Fisher Scientific) as previously described [48].

Pyrene actin polymerization assay

To probe actin polymerization, 100 nM SPIN90-Cter and 10 nM Arp2/3 iso-complexes were mixed with 2.5 μM Actin (5% pyrene labelled) and loaded immediately on a Safas Xenius fluorimeter. The negative control experiment was done without SPIN90-Cter. The experiments were performed at room temperature with a buffer containing 5 mM Tris-HCl pH 7.0, 0.1 mM CaCl2, 0.2 mM ATP, 50 mM KCl, 1 mM $MgCl_2$, 0.2 mM EGTA and 1 mM DTT.

TIRF assays

The coverslips were treated with Deep UV and passivated by mPEG silane overnight. The passivated coverslips were rinsed thoroughly with ethanol and water. Then they were dried and stuck to the glass slides with 3-mm-separated parafilm bands to create flow chambers. The experiments were performed at 25 °C. To begin with, 200 nM SPIN90-Cter, 20 nM Arp2/3 iso-complexes were mixed in a buffer containing 5 mM Tris-HCl pH 7.0, 50 mM KCl, 1 mM $MgCl_2$, 0.2 mM EGTA, 0.2 mM ATP, 10 mM DTT, 1 mM DABCO, 0.1% BSA, and 0.3% Methylcellulose 4000 cP. The moment when 0.5 μM G-actin (15% Alexa-488 labelled) was added to the system was recorded as time 0. Negative control experiments were performed using the same system, either without SPIN90-Cter or with actin alone. For each condition, a random field of view was selected to quantify actin density. Actin density was quantified as the number of actin filaments divided by the surface area of the selected region.

GST pull-down assays

The Glutathione Sepharose™ 4B resin (GE Healthcare) was incubated with 5% BSA for 5 min and washed three times with GST pull-down buffer containing 50 mM Tris-HCl pH 7.0, 50 mM KCl, 1 mM $MgCl_2$, 0.2 mM EGTA, 0.2 mM ATP, 1 mM DTT, and 5% glycerol. The

641 beads were then incubated with 20 μM GST-SPIN90-Cter or 20 μM GST at 4 °C for 1h,
642 followed by incubation with 100 nM Arp2/3 iso-complexes at 4 °C for 30 min. The beads
643 were washed three times with 300 μL GST pull-down buffer. The proteins attached to the
644 beads were eluted with 50 μL of 50 mM reduced glutathione. The sample was analyzed
645 by SDS-PAGE followed by western blot using Anti-ArpC2 (sigma) to detect Arp2/3
646 complexes. Amersham imager AI600 or ImageQuant™ 800 was used to develop the
647 western blot results. To quantify the affinity between SPIN90 and Arp2/3 iso-complexes,
648 we focused on Arp2/3-ArpC1B-ArpC5 and Arp2/3-ArpC1B-ArpC5L. To quantify the
649 dissociation rate of the Arp2/3 complex from SPIN90, equal amounts of SPIN90-coated
650 GST beads were incubated with 2 μM Arp2/3 iso-complexes. Unbound Arp2/3 complexes
651 were removed after the initial incubation. The beads were then washed and eluted at
652 various time points. The amount of eluted Arp2/3 was analyzed by western blot. The blot
653 is auto-exposed to improve resolution, as the exposure time for the sample containing
654 ArpC5 is consistently much longer than that for ArpC5L. To quantify the dissociation
655 constant, equal amounts of SPIN90-coated GST beads were incubated with varying
656 concentrations of Arp2/3 iso-complexes. The amounts of eluted Arp2/3-ArpC5 and
657 Arp2/3-ArpC5L were loaded onto the same gel and transferred to the same western blot
658 membrane. The developed western blot was analyzed using FIJI with plugin GelAnalyzer.
659 The experiments were repeated independently three times, and all the results were
660 included in the final plot (Fig. 2C).
661
662 **Antibody, immunoblot analysis**
663 The antibody against mouse SPIN90 (UniProt Q9ESJ4) was generated by immunizing
664 rabbits with full-length purified recombinant mouse SPIN90 protein (WhiteAntibodies).
665 Other antibodies are including: ARPC2/p34-Arc polyclonal (Millipore, 07-227), ARPC5
666 monoclonal (Synaptic Systems, 305011), ArpC5L (Proteintech, 22025-a-AP), β-actin
667 (Abcam, ab179467), anti-mouse IgG-IRDye® 800CW (LI-COR Biosciences, 926-32210)
668 and anti-rabbit IgG-IRDye® 680RD (LI-COR Biosciences, 926-68071). Unless otherwise
669 specified, western blot results were developed on LI-COR Odyssey CLx imaging
670 system. FIJI with plugin GelAnalyzer was used to analyse the results.
671
672 **Cell culture and cell lines**
673 WT M. Musculus B16-F1melanoma cells were gifts from Klemens Rottner lab [39]. Unless
674 otherwise specified in this project, cells were cultured in Gibco DMEM (ThermoFisher,
675 41966-029) with additional 10% FBS (CAPRICORN, FBS-LE-12A) and 1% Penicillin-
676 Streptomycin (P/S, ThermoFisher, 15140122) at 37°C and 5% CO_2. To detach the cells,
677 cells were washed with PBS once and then treated with 0.25% Trypsin-EDTA
678 (ThermoFisher, 25200056) at room temperature for 2-3 minutes.

679 ArpC5, ArpC5L and SPIN90 KO cell lines were generated by GRSPR-Cas9-mediated
680 genome editing approaches. In each case, to generate a cut in the target gene, a pair of

681 guide RNA were cloned intro pSpCas9(BB)-2A-Puro (Addgene, ID 48139) respectively and
682 introduced into B16-F1 at the same time. The ArpC5 guide RNAs are
683 'GACCGGGCTGGGCTCGCTAA' and 'GCGAGGTGGACTCGTGCCTA'. The guide RNAs
684 against ArpC5L are 'ATTCGTCGATATCCACGCGG' and 'CGGCAATATCCTTCCCGGCG'.
685 The SPIN90 guide RNAs are 'GAGAGCCTAGAAGTCTGCAT' and
686 'GCTCCGTGGTGTCCATTGGA'. Cells were transfected using Fugene® HD Transfection
687 Reagent. The next day, cells were selectively cultured by introducing 2.5 μg/mL
688 puromycin into the medium. After 3 days, surviving cells were trypsinized and
689 resuspended in PBS with additional 5% FBS. The single cells were sorted by the flow
690 cytometry and seeded in DMEM with additional 20% FBS and 1% P/S in 96 well plates.
691 Two weeks later, single colonies were expanded for characterizing, including Western
692 blot and genomic sequencing of the target loci.

693 ArpC5 and ArpC5L genes were modified using ORANGE, a CRISPR-Cas9–mediated
694 genome editing toolbox to fuse a NeonGreen tag with the target gene [49]. pOrange
695 NeonGreen-ArpC5 KI plasmid was modified based on pOrange GFP-ArpC5 KI (Addgene
696 #131503). pOrange ArpC5L-NeonGreen KI plasmid was generated using the guide RNA:
697 'CAGTGTGTTCCGGGCCATGG'. The same method was used to generate endogenously
698 GFP-tagged β-actin. The plasmid pOrange GFP-Actb KI (Addgene #131479) was
699 transfected into the WT, ArpC5 isoform KO, SPIN90 KO cells respectively. Single cells
700 with green fluorescence were sorted by flow cytometry and seeded into 96-well plates
701 containing DMEM supplemented with 20% FBS and 1% P/S. Expanded single colonies
702 were examined by Western blot. All the positive clones we tested (approximately 10 for
703 each condition) were heterozygous.
704
705 B16 cells overexpressing GFP was generated using lentivirus infection (Trono group
706 second generation packaging system, Addgene) and selected using puromycin
707 resistance (1 μg/mL) as previously described [22].
708
709 **siRNA transfection**
710 All-Star control (Qiagen, SI03650318) was used as the control. The following RNAi were
711 purchased from Dharmacon (SMARTPools): siGENOME mouse ArpC5 (NM_026369),
712 siGENOME mouse ArpC5L (NM_028809), siGENOME mouse NCKIPSD/SPIN90
713 (NM_030729). The final concentration of 20 nM was used. The cells were transfected with
714 HiPerFect (Qiagen) using the fast forward method in 6-well plates. The experiments were
715 performed 48h after the transfection. At the same time, the depletion of target gene were
716 examined with Western Blot.
717
718 **Immunofluorescence on fixed cells**
719 B16 cells were seeded on laminin coated coverslips as previously reported [25], and
720 cultured in CO_2 independent medium (Gibco™) with additional 10% FBS and 2 mM L-

721 Glutamine at 37°C. After 3h30 incubation, the cells were fixed with 4% PFA in PBS at
722 37°C. After fixation, cells were washed three times with warm PBS and permeabilized
723 with 0.1% Triton X-100 in PBS for 1 min. Permeabilized cells were incubated with primary
724 antibody for 40 minutes and secondary antibody for 40 minutes at room temperature
725 (around 25°C). The samples were mounted with Mowiol (sigma). The coverslips were
726 imaged on a Zeiss Axioplan2 microscope controlled with MetaMorph 7.8.13.0 software.
727 A 63x/1.4 NA Plan-Achromat objective and a Photometrics Cool Snap HQ cooled charge-
728 coupled device camera were used.
729
730 **Polarized fluorescence microscopy on fixed cells**
731 B16 cells were seeded on laminin coated coverslips as previously reported [25], and
732 cultured in CO_2 independent medium (Gibco™) with additional 10% FBS and 2 mM L-
733 Glutamine at 37°C. After 3h30 incubation, the cells were fixed with 0.35% glutaraldehyde
734 and 4% PFA in cytoskeleton buffer at 37°C, as reported [50]. The samples were washed
735 twice with PBS containing 1 mg/mL sodium borohydride and three times with PBS. The
736 actin cytoskeleton was stained with 0.22 µM Phalloidin Alexa-488 at room temperature
737 for 2 h in PBS containing 0.1% saponin and 10% BSA. The samples were mounted with
738 Mowiol and kept at 4 °C.
739
740 The images were acquired using a custom spinning disk polarization-resolved
741 fluorescence microscope with a Nikon Plan Apo ×100/1.45 NA oil immersion objective
742 lens, 488- and 561-laser lines and an iXon Ultra 888 EMCCD camera, described in detail
743 in Martins et al, 2025. Polarized image stacks using 18 polarization angles with steps of
744 10° were recorded with an exposure time of 0.3-0.4 s per polarized image. Analysis and
745 data representation, including color-coded stick representations of ρ angles with
746 respect to the leading edge (ρ_c) and of ψ angles per pixel, histograms and polar
747 histograms were generated with the open source PyPOLAR software (RRID:SCR_024681)
748 (Martins et al, 2025). Pixels of the lamellipodia selected for analysis were identified using
749 a combination of intensity thresholding and the "edge detection" tool in PyPOLAR to
750 detect the leading edge and manual region selection, excluding microspikes. Only 10
751 pixels (0.65 µm) from the leading edge were included for analysis.
752
753 **Live cell imaging**
754 The siRNA treated NeonGreen-ArpC5 and ArpC5L-NeonGreen cells were seeded on
755 laminin-coated coverslips in Leibovitz's L-15 medium supplemented with 10% FBS and
756 2 mM L-glutamine at 37 °C. After 3-hour incubation, the cells were imagined on a Zeiss
757 Axio Observer spinning disc with a Plan Achromat 100x/1.46 NA oil lens, an Evolve 512
758 camera, and a Yokagawa CSUX spinning disk. The microscope was controlled by the
759 SlideBook software (3i Intelligent imaging Innovations). For each condition, more than 8
760 cells with lamellipodia were chosen randomly. The same exposure time, 200 ms, was
761 applied in each acquisition. Similarly, WT and KO cells expressing endogenous GFP-β-

actin were seeded and imagined on the confocal spinning disc with a Plan Achromat 100x/1.46 NA oil lens. Life images were acquired at 5 second intervals. A region of interest on the lamellipodia was photobleached using a focused 3-ms pulse of a 405 nm laser. Images were analyzed using FIJI software with Multi Kymograph.

Ruby-tagged SPIN90 was transiently introduced into cells using the FuGENE kit 48 hours before the experiment. The ArpC5L-NeonGreen or GFP overexpressing Ruby-tagged SPIN90 cells were seeded on laminin-coated coverslips in Leibovitz's L-15 medium supplemented with 10% FBS and 2 mM L-glutamine at 37 °C. After 3 hours, the cells were imagined using instant Structured Illumination Microscopy (VT-iSIM). VT-iSIM was conducted on an Olymus iX83 Microscope with Olympus 150x/1.45 NA X-Line apochromatic objective lens, dual Photometrics BSI-Express sCMOS cameras, and CoolLED pE-300 light source (Visitech), controlled using Micro-Manager. Images were acquired at 1 second intervals with 200 ms exposure time. Images were analyzed using FIJI software. Normalized fluorescent signal intensity at the leading edge was quantified by dividing the intensity at the leading edge (solid line, Fig. 3A) by the intensity measured 2 µm behind the leading edge (dashed line, Fig. 3A).

To quantify the random motility, WT and CRISPR KO cells were imaged and analysed using the Livecyte system (PhaseFocus) every 10 minutes for 16 hours at 10x. The imaging chamber was maintained at 37 °C with 5% CO_2. Livecyte automatically process the data and quantified the cell motility.

Protein structure analysis

Pymol is used to visualise and analyse the structure of SPIN90 bound Arp2/3 [51].

Statistical analysis

Statistical analyses were performed with Prism 10 (Version 10.1.1). Sample numbers, mean and P value can be found in the figures or figure legends. Unless otherwise specified, each experiment have been independently repeated three times. P-values smaller than 0.05 are considered statistically significant. Moreover, Cohen's d was also used to assess the effect size; a Cohen's d greater than 0.8 is considered a large effect. Cells receiving the treatment (e.g., siRNA) on the same day were paired. A paired two-tailed Student's t-test was then used to compare the means between the two groups. Also, a paired two-tailed Student's *t*-test was used to compare the signal intensity of GFP and Ruby SPIN90 at the leading edge. Because the data distribution in the polarized microscopy assay differs substantially, we used an unpaired two-tailed *t*-test with Welch's correction or Mann Whitney test to compare the two groups. A paired two-tailed *t*-test with was used to compare lamellipodia protrusion between wild type and KO cell lines.

Supplementary:

Sequence results:

The grey colored fragment is present in WT cell lines but missing in KO cells.

B16-F1 ArpC5 knockout lines

Reference: MmC5 WT

CCGGGCTGGGCTCGCTAAAGGAGAGGCACCGCGGAGGGGCAGGCCAGCGTCGCGTC
GCGATCCGGGATGTCGAAGAACACGGTGTCGTCGGCCCGCTTCCGGAAGGTGGACGTG
GACGAATATGACGAGAACAAGTTCGTGGACGAGGAGGACGGCGGCGATGGCCAGGCC
GGGCCCGACGAGGGCGAGGTGGACTCGTGCCTACGGCAATATC

MmC5 KO 2.1

CCGGGCTGGGCTCGCGCGGCAATATC

B16-F1 ArpC5L Knockout lines

Reference: MmC5L WT

CGCTTCCGCCGCGTGGATATCGACGAATTTGACGAGAACAAATTCGTAGACGAGCACGAA
GAGGCAGCGGCGGCGGCGGGCGAGCCAGGCCCCGACCCCTGCGAGGTAGACGGGC
TCCTGCGGCAATATCCTTCCCGGCGCGGCGGCCCGGCT

MmC5L KO 2.2

CGCTTCCGCCGCGTGGCGCGGCGGCCCGGCT

B16-F1 SPIN90 Knockout lines

Reference: SPIN90 WT

GAGGATGGCCTTCCAATGGACACCACGGAGCAGCTGCCAGACCTCTGCATGAACCTGCT
TCTGGCTCTCAACCTGCACCTGACAGGTGGGGTGGGGCCATCTGGAAGGCAGCTGAGC
AGTGGGCTTTTCGGGCTTCGCGGGCTTCTGTGCCTACACTCTTACCTGTCTCCATCCACGT
CTCTCCGCAGCTCCTGAGCAGAATGTCATCATGGCTGCCTTGAGCAGACACACCAATGTG
AAGATCTTCTCTGAGAAGCTGCTTCTGCTTCTGAACAGAGGGGGTGAGAGCCTAGAAGTCT
GCATGGGTGCCGCTTGCGT

SPIN90 KO 2.10

GAGGATGGCCTTCCCATGGGTGCCGCTTGCGT

References

1 Machesky, L. M. *et al*. Mammalian actin-related protein 2/3 complex localizes to regions of lamellipodial protrusion and is composed of evolutionarily conserved proteins. *Biochem J* **328 (Pt 1)**, 105-112, doi:10.1042/bj3280105 (1997).

2 Papalazarou, V. & Machesky, L. M. The cell pushes back: The Arp2/3 complex is a key orchestrator of cellular responses to environmental forces. *Curr Opin Cell Biol* **68**, 37-44, doi:10.1016/j.ceb.2020.08.012 (2021).

3 Welch, M. D., DePace, A. H., Verma, S., Iwamatsu, A. & Mitchison, T. J. The human Arp2/3 complex is composed of evolutionarily conserved subunits and is

localized to cellular regions of dynamic actin filament assembly. *J Cell Biol* **138**, 375-384, doi:10.1083/jcb.138.2.375 (1997).

4 Stradal, T. E. B., Boiero Sanders, M. & Bieling, P. Arp2/3-complex regulation - Novel insights and open questions. *Curr Opin Cell Biol* **95**, 102565, doi:10.1016/j.ceb.2025.102565 (2025).

5 Cao, L. & Way, M. The stabilization of Arp2/3 complex generated actin filaments. *Biochem Soc Trans*, doi:10.1042/BST20230638 (2024).

6 Gautreau, A. M., Fregoso, F. E., Simanov, G. & Dominguez, R. Nucleation, stabilization, and disassembly of branched actin networks. *Trends Cell Biol* **32**, 421-432, doi:10.1016/j.tcb.2021.10.006 (2022).

7 Mullins, R. D., Heuser, J. A. & Pollard, T. D. The interaction of Arp2/3 complex with actin: nucleation, high affinity pointed end capping, and formation of branching networks of filaments. *Proc Natl Acad Sci U S A* **95**, 6181-6186, doi:10.1073/pnas.95.11.6181 (1998).

8 Wagner, A. R., Luan, Q., Liu, S. L. & Nolen, B. J. Dip1 defines a class of Arp2/3 complex activators that function without preformed actin filaments. *Curr Biol* **23**, 1990-1998, doi:10.1016/j.cub.2013.08.029 (2013).

9 Espinoza-Sanchez, S., Metskas, L. A., Chou, S. Z., Rhoades, E. & Pollard, T. D. Conformational changes in Arp2/3 complex induced by ATP, WASp-VCA, and actin filaments. *Proc Natl Acad Sci U S A* **115**, E8642-E8651, doi:10.1073/pnas.1717594115 (2018).

10 Smith, B. A. *et al.* Three-color single molecule imaging shows WASP detachment from Arp2/3 complex triggers actin filament branch formation. *Elife* **2**, e01008, doi:10.7554/eLife.01008 (2013).

11 Molinie, N. *et al.* Cortical branched actin determines cell cycle progression. *Cell Res* **29**, 432-445, doi:10.1038/s41422-019-0160-9 (2019).

12 Luan, Q., Liu, S. L., Helgeson, L. A. & Nolen, B. J. Structure of the nucleation-promoting factor SPIN90 bound to the actin filament nucleator Arp2/3 complex. *EMBO J* **37**, doi:10.15252/embj.2018100005 (2018).

13 Cao, L. *et al.* SPIN90 associates with mDia1 and the Arp2/3 complex to regulate cortical actin organization. *Nat Cell Biol* **22**, 803-814, doi:10.1038/s41556-020-0531-y (2020).

14 Hinze, C. & Boucrot, E. Endocytosis in proliferating, quiescent and terminally differentiated cells. *J Cell Sci* **131**, doi:10.1242/jcs.216804 (2018).

15 Schrank, B. R. *et al.* Nuclear ARP2/3 drives DNA break clustering for homology-directed repair. *Nature* **559**, 61-66, doi:10.1038/s41586-018-0237-5 (2018).

16 Wu, C. *et al.* Arp2/3 is critical for lamellipodia and response to extracellular matrix cues but is dispensable for chemotaxis. *Cell* **148**, 973-987, doi:10.1016/j.cell.2011.12.034 (2012).

17 Balzer, C. J., Wagner, A. R., Helgeson, L. A. & Nolen, B. J. Single-Turnover Activation of Arp2/3 Complex by Dip1 May Balance Nucleation of Linear versus

885 Branched Actin Filaments. *Curr Biol* **29**, 3331-3338 e3337,
886 doi:10.1016/j.cub.2019.08.023 (2019).
887 18 Eisenmann, K. M. *et al.* Dia-interacting protein modulates formin-mediated actin
888 assembly at the cell cortex. *Curr Biol* **17**, 579-591,
889 doi:10.1016/j.cub.2007.03.024 (2007).
890 19 Robinson, R. C. *et al.* Crystal structure of Arp2/3 complex. *Science* **294**, 1679-
891 1684, doi:10.1126/science.1066333 (2001).
892 20 Jay, P. *et al.* ARP3beta, the gene encoding a new human actin-related protein, is
893 alternatively spliced and predominantly expressed in brain neuronal cells. *Eur J*
894 *Biochem* **267**, 2921-2928, doi:10.1046/j.1432-1327.2000.01306.x (2000).
895 21 Millard, T. H., Behrendt, B., Launay, S., Futterer, K. & Machesky, L. M.
896 Identification and characterisation of a novel human isoform of Arp2/3 complex
897 subunit p16-ARC/ARPC5. *Cell Motil Cytoskeleton* **54**, 81-90,
898 doi:10.1002/cm.10087 (2003).
899 22 Abella, J. V. *et al.* Isoform diversity in the Arp2/3 complex determines actin
900 filament dynamics. *Nat Cell Biol* **18**, 76-86, doi:10.1038/ncb3286 (2016).
901 23 Roman, W. *et al.* Myofibril contraction and crosslinking drive nuclear movement
902 to the periphery of skeletal muscle. *Nat Cell Biol* **19**, 1189-1201,
903 doi:10.1038/ncb3605 (2017).
904 24 Sadhu, L. *et al.* ARPC5 isoforms and their regulation by calcium-calmodulin-N-
905 WASP drive distinct Arp2/3-dependent actin remodeling events in CD4 T cells.
906 *Elife* **12**, doi:10.7554/eLife.82450 (2023).
907 25 Fassler, F. *et al.* ArpC5 isoforms regulate Arp2/3 complex-dependent protrusion
908 through differential Ena/VASP positioning. *Sci Adv* **9**, eadd6495,
909 doi:10.1126/sciadv.add6495 (2023).
910 26 Kahr, W. H. *et al.* Loss of the Arp2/3 complex component ARPC1B causes
911 platelet abnormalities and predisposes to inflammatory disease. *Nat Commun*
912 **8**, 14816, doi:10.1038/ncomms14816 (2017).
913 27 Volpi, S. *et al.* A combined immunodeficiency with severe infections,
914 inflammation, and allergy caused by ARPC1B deficiency. *J Allergy Clin Immunol*
915 **143**, 2296-2299, doi:10.1016/j.jaci.2019.02.003 (2019).
916 28 Sindram, E. *et al.* ARPC5 deficiency leads to severe early-onset systemic
917 inflammation and mortality. *Dis Model Mech* **16**, doi:10.1242/dmm.050145
918 (2023).
919 29 Vasconcellos, L., Huang, S., Suarez-Bonnet, A., Priestnall, S. & Sunita Varsani-
920 Brown, M. L. W., Kathleen Shah, Naoko Kogata, Brigitta Stockinger, Michael Way.
921 Branched actin networks in innate immune cells mediate host microbiota
922 homeostasis. *BioRXiv* (2024).
923 30 Nunes-Santos, C. J. *et al.* Inherited ARPC5 mutations cause an actinopathy
924 impairing cell motility and disrupting cytokine signaling. *Nat Commun* **14**, 3708,
925 doi:10.1038/s41467-023-39272-0 (2023).

31 von Loeffelholz, O. *et al.* Cryo-EM of human Arp2/3 complexes provides structural insights into actin nucleation modulation by ARPC5 isoforms. *Biol Open* **9**, doi:10.1242/bio.054304 (2020).
32 Saks, A. J., Barrie, K. R., Rebowski, G. & Dominguez, R. NPF binding to Arp2 is allosterically linked to the release of ArpC5's N-terminal tail and conformational changes in Arp2/3 complex. *Proc Natl Acad Sci U S A* **122**, e2421557122, doi:10.1073/pnas.2421557122 (2025).
33 Cao, L., Huang, S., Basant, A., Mladenov, M. & Way, M. CK-666 and CK-869 differentially inhibit Arp2/3 iso-complexes. *EMBO Rep* **25**, 3221-3239, doi:10.1038/s44319-024-00201-x (2024).
34 Galloni, C. *et al.* MICAL2 enhances branched actin network disassembly by oxidizing Arp3B-containing Arp2/3 complexes. *J Cell Biol* **220**, doi:10.1083/jcb.202102043 (2021).
35 Liu, T. *et al.* Arp2/3-mediated bidirectional actin assembly by SPIN90 dimers. *Nat Struct Mol Biol* **32**, 2262-2271, doi:10.1038/s41594-025-01665-8 (2025).
36 Francis, J. *et al.* Activation of Arp2/3 complex by a SPIN90 dimer in linear actin-filament nucleation. *Nat Struct Mol Biol* **32**, 2272-2284, doi:10.1038/s41594-025-01673-8 (2025).
37 Francis, J. *et al.* Activation of Arp2/3 complex by a SPIN90 dimer in linear actin-filament nucleation. *Nat Struct Mol Biol*, doi:10.1038/s41594-025-01673-8 (2025).
38 Liu, T. *et al.* Arp2/3-mediated bidirectional actin assembly by SPIN90 dimers. *Nat Struct Mol Biol*, doi:10.1038/s41594-025-01665-8 (2025).
39 Lai, F. P. *et al.* Arp2/3 complex interactions and actin network turnover in lamellipodia. *EMBO J* **27**, 982-992, doi:10.1038/emboj.2008.34 (2008).
40 Steffen, A. *et al.* Sra-1 and Nap1 link Rac to actin assembly driving lamellipodia formation. *EMBO J* **23**, 749-759, doi:10.1038/sj.emboj.7600084 (2004).
41 Martins, C. S. *et al.* Genetically encoded reporters of actin filament organization in living cells and tissues. *Cell* **188**, 2540-2559 e2527, doi:10.1016/j.cell.2025.03.003 (2025).
42 Watanabe, N. & Mitchison, T. J. Single-molecule speckle analysis of actin filament turnover in lamellipodia. *Science* **295**, 1083-1086, doi:10.1126/science.1067470 (2002).
43 Giannone, G. *et al.* Lamellipodial actin mechanically links myosin activity with adhesion-site formation. *Cell* **128**, 561-575, doi:10.1016/j.cell.2006.12.039 (2007).
44 Baldauf, L., Frey, F., Arribas Perez, M., Idema, T. & Koenderink, G. H. Branched actin cortices reconstituted in vesicles sense membrane curvature. *Biophys J* **122**, 2311-2324, doi:10.1016/j.bpj.2023.02.018 (2023).
45 Spudich, J. A. & Watt, S. The regulation of rabbit skeletal muscle contraction. I. Biochemical studies of the interaction of the tropomyosin-troponin complex with

actin and the proteolytic fragments of myosin. *J Biol Chem* **246**, 4866-4871 (1971).

46 Cao, L., Ghasemi, F., Way, M., Jegou, A. & Romet-Lemonne, G. Regulation of branched versus linear Arp2/3-generated actin filaments. *EMBO J* **42**, e113008, doi:10.15252/embj.2022113008 (2023).

47 Romet-Lemonne, G., Guichard, B. & Jegou, A. Using Microfluidics Single Filament Assay to Study Formin Control of Actin Assembly. *Methods Mol Biol* **1805**, 75-92, doi:10.1007/978-1-4939-8556-2_4 (2018).

48 Cooper, J. A., Walker, S. B. & Pollard, T. D. Pyrene actin: documentation of the validity of a sensitive assay for actin polymerization. *J Muscle Res Cell Motil* **4**, 253-262, doi:10.1007/BF00712034 (1983).

49 Willems, J. *et al.* ORANGE: A CRISPR/Cas9-based genome editing toolbox for epitope tagging of endogenous proteins in neurons. *PLoS Biol* **18**, e3000665, doi:10.1371/journal.pbio.3000665 (2020).

50 Rimoli, C. V., Valades-Cruz, C. A., Curcio, V., Mavrakis, M. & Brasselet, S. 4polar-STORM polarized super-resolution imaging of actin filament organization in cells. *Nat Commun* **13**, 301, doi:10.1038/s41467-022-27966-w (2022).

51 Schrodinger, LLC. *The PyMOL Molecular Graphics System, Version 1.8* (2015).

A

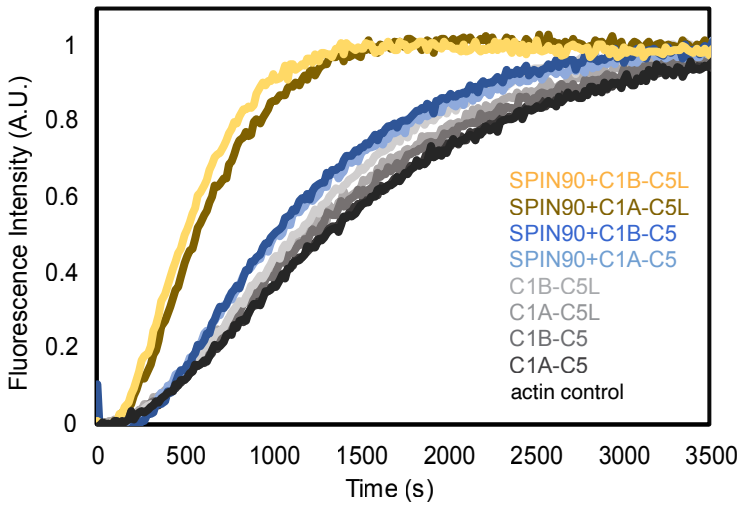

B

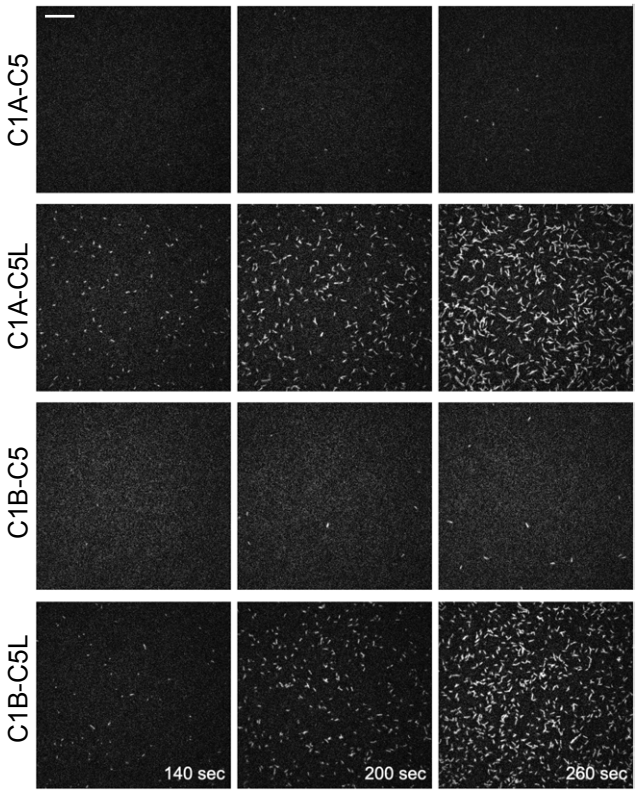

Scale bar = 20 µm

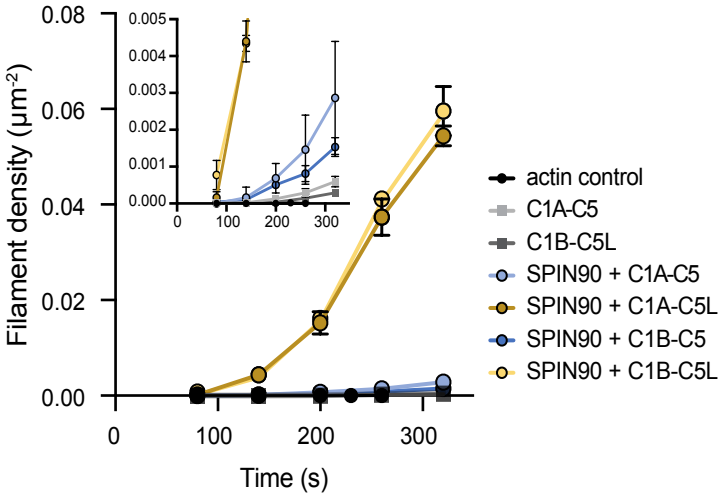

Figure 1

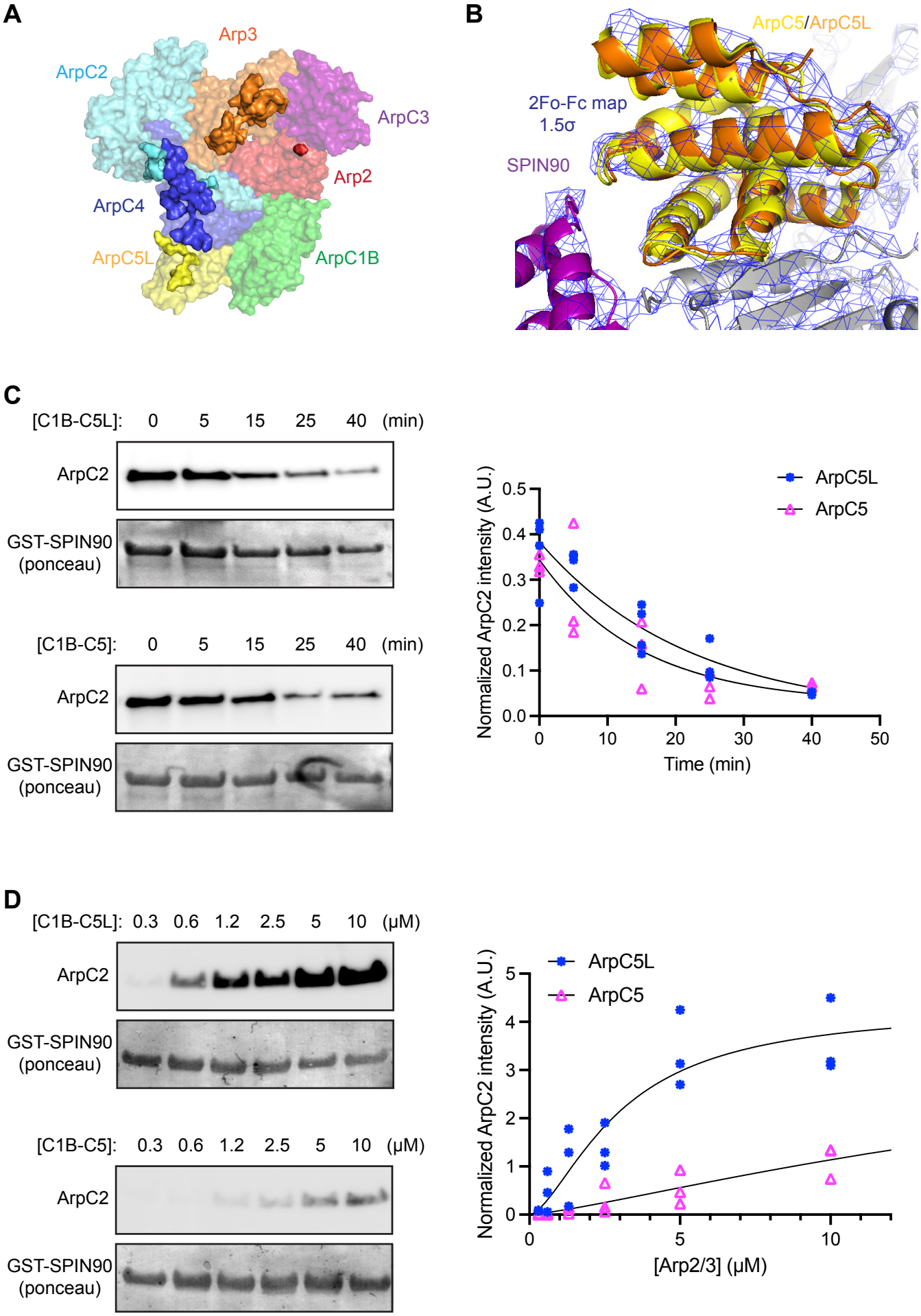
A
Arp3
ArpC2
ArpC3
Arp2
ArpC4
ArpC5L
ArpC1B
B
ArpC5/ArpC5L
2Fo-Fc map
1.5σ
SPIN90
C
[C1B-C5L]: 0 5 15 25 40 (min)
ArpC2
GST-SPIN90
(ponceau)
[C1B-C5]: 0 5 15 25 40 (min)
ArpC2
GST-SPIN90
(ponceau)
ArpC5L
ArpC5
Normalized ArpC2 intensity (A.U.)
Time (min)
D
[C1B-C5L]: 0.3 0.6 1.2 2.5 5 10 (μM)
ArpC2
GST-SPIN90
(ponceau)
[C1B-C5]: 0.3 0.6 1.2 2.5 5 10 (μM)
ArpC2
GST-SPIN90
(ponceau)
ArpC5L
ArpC5
Normalized ArpC2 intensity (A.U.)
[Arp2/3] (μM)

A

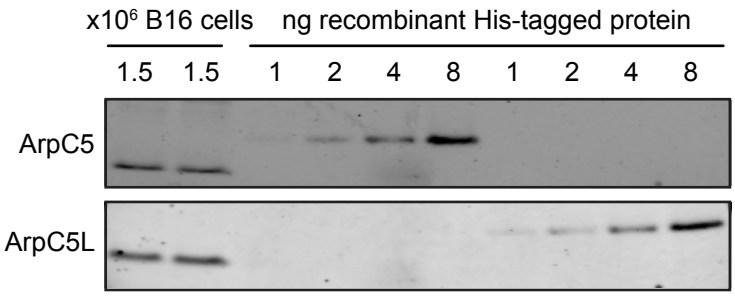

	ArpC5	ArpC5L
nmol/cell ± SD	1.25×10^{-6} 2.0×10^{-7}	2.1×10^{-6} 5.6×10^{-7}

B

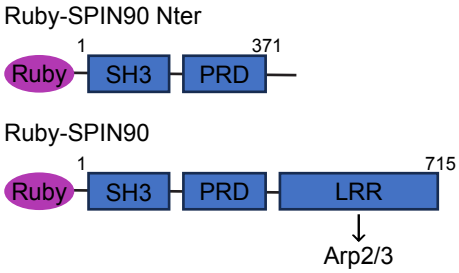

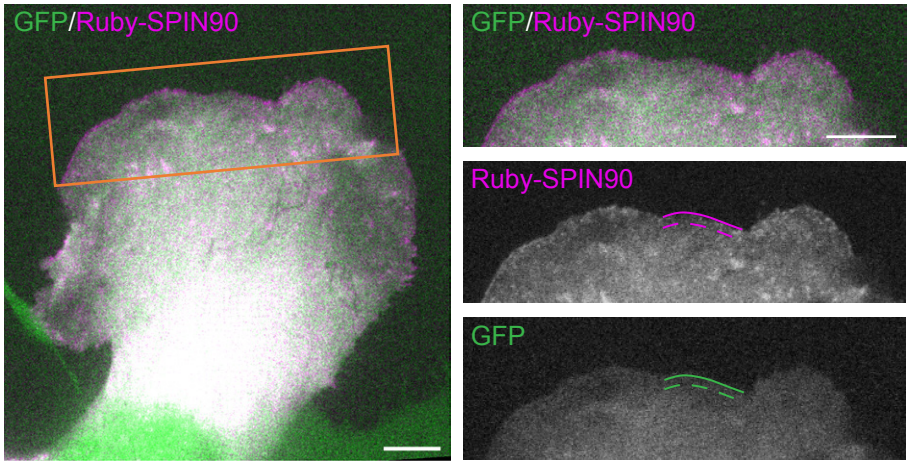

Scale bar = 5 µm

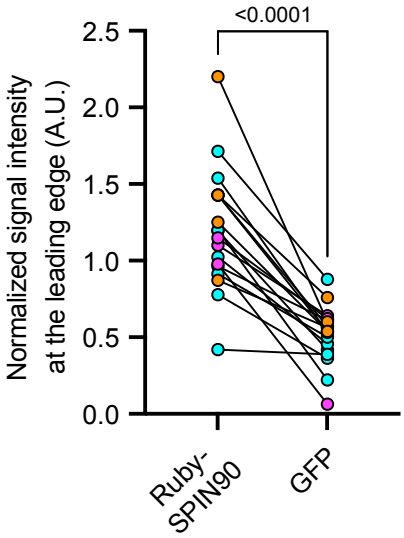

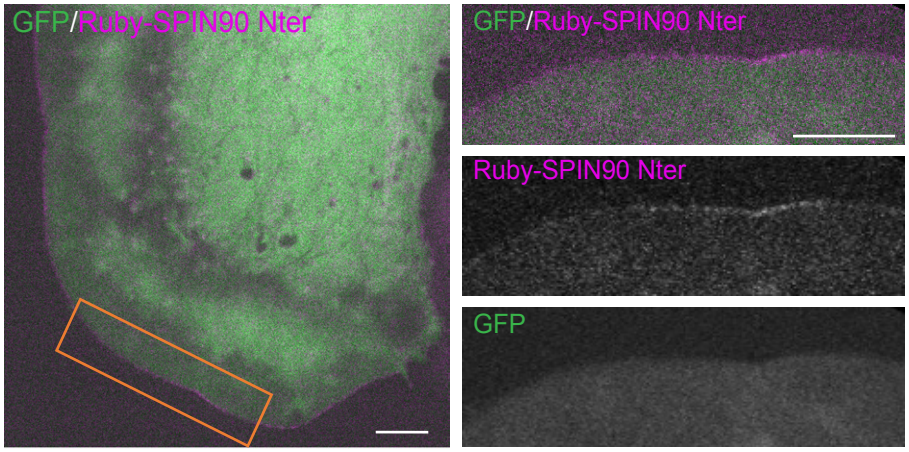

Scale bar = 5 µm

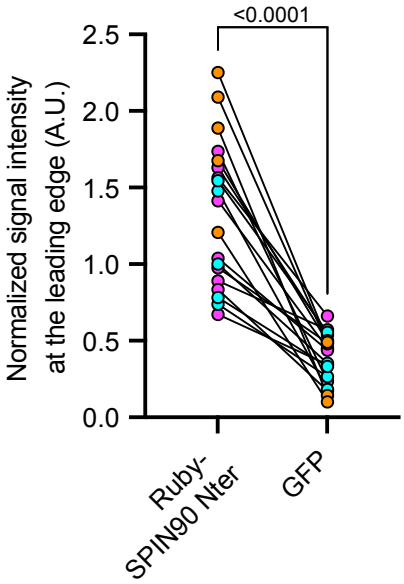

Figure 3

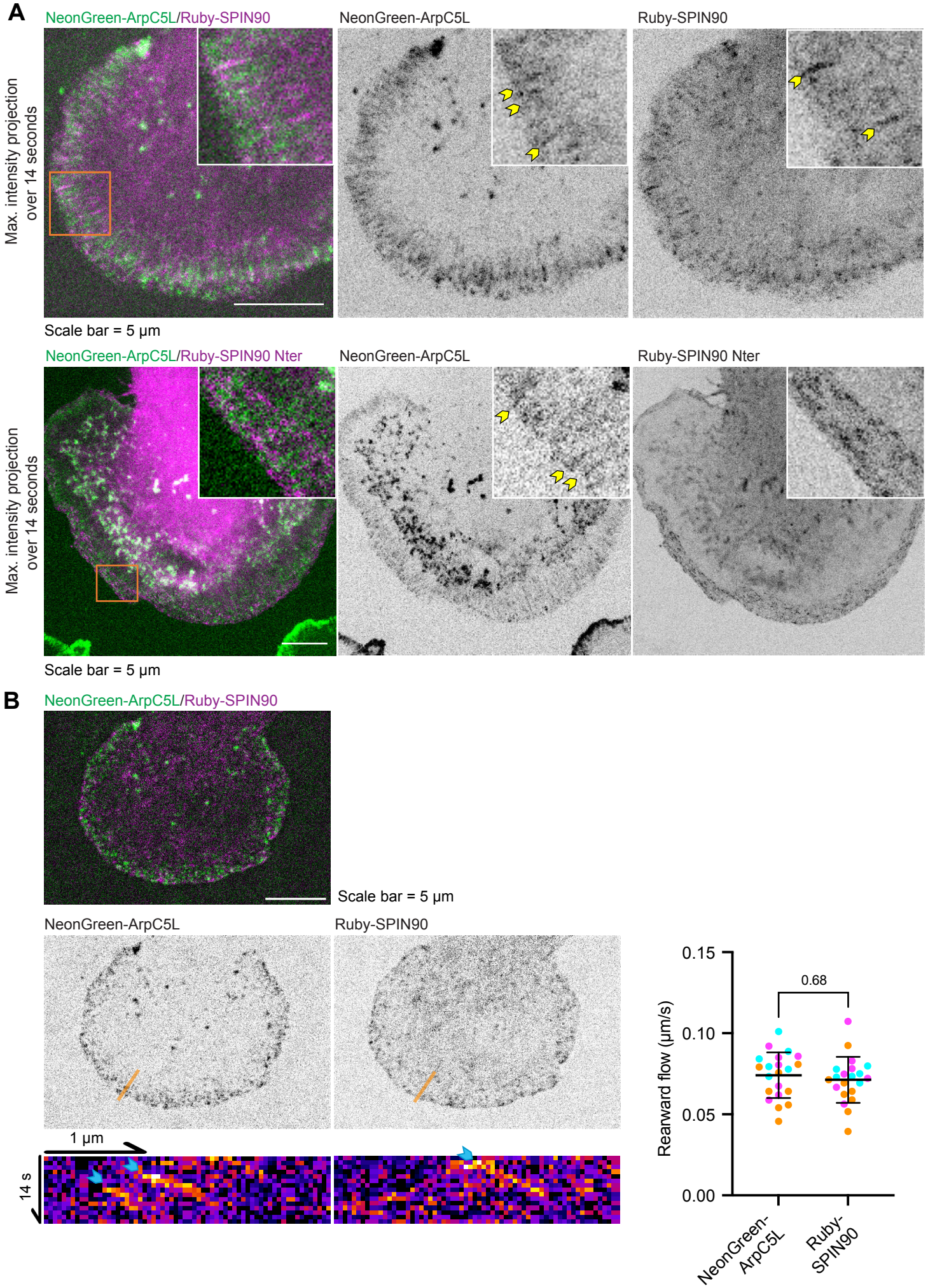
A
NeonGreen-ArpC5L/Ruby-SPIN90
NeonGreen-ArpC5L
Ruby-SPIN90
Max. intensity projection over 14 seconds
Scale bar = 5 µm
NeonGreen-ArpC5L/Ruby-SPIN90 Nter
NeonGreen-ArpC5L
Ruby-SPIN90 Nter
Max. intensity projection over 14 seconds
Scale bar = 5 µm
B
NeonGreen-ArpC5L/Ruby-SPIN90
Scale bar = 5 µm
NeonGreen-ArpC5L
Ruby-SPIN90
1 µm
14 s
Rearward flow (µm/s)
0.15
0.10
0.05
0.00
0.68
NeonGreen-ArpC5L
Ruby-SPIN90

Figure 4

A

NeonGreen-ArpC5L

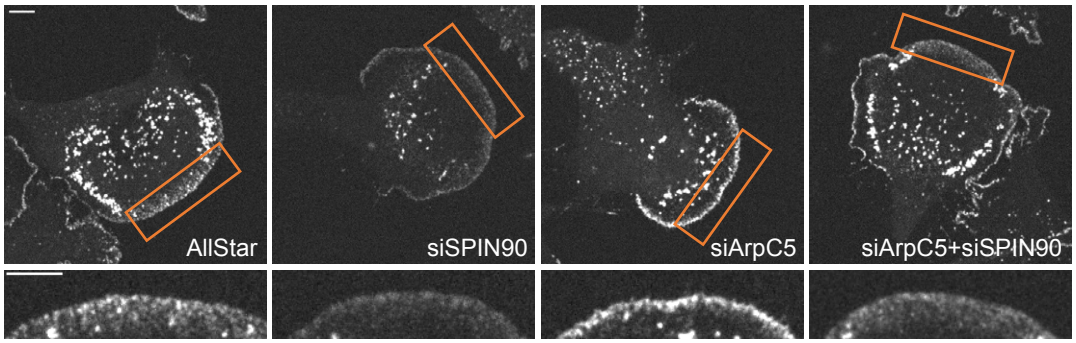

Scale bar = 5 µm

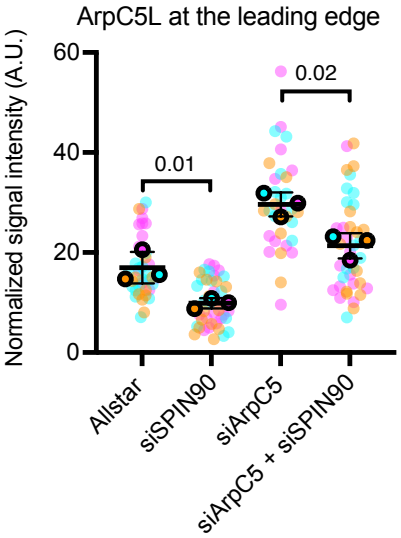

B

ArpC5-NeonGreen

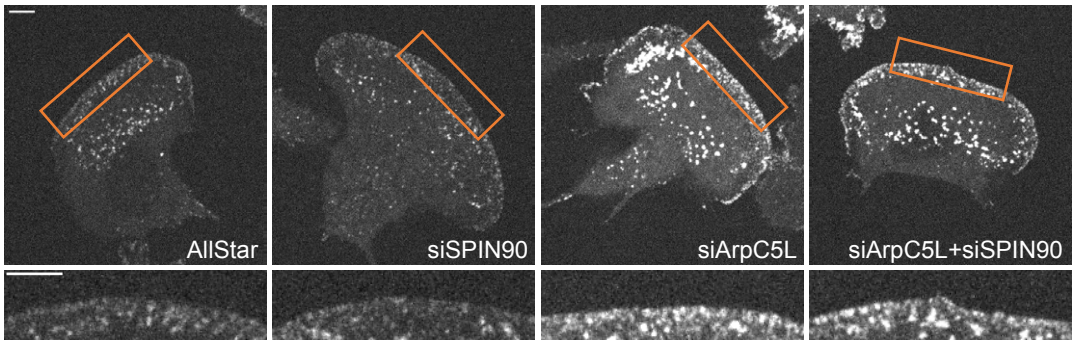

Scale bar = 5 µm

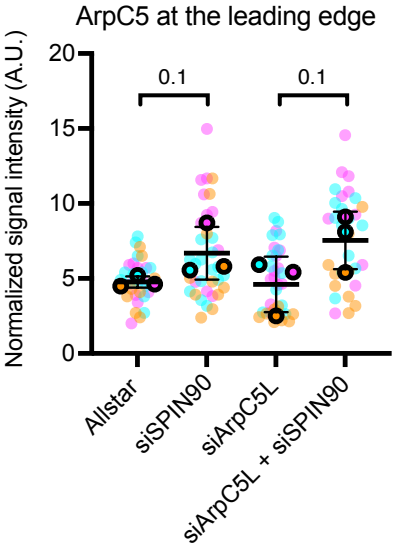

Figure 5

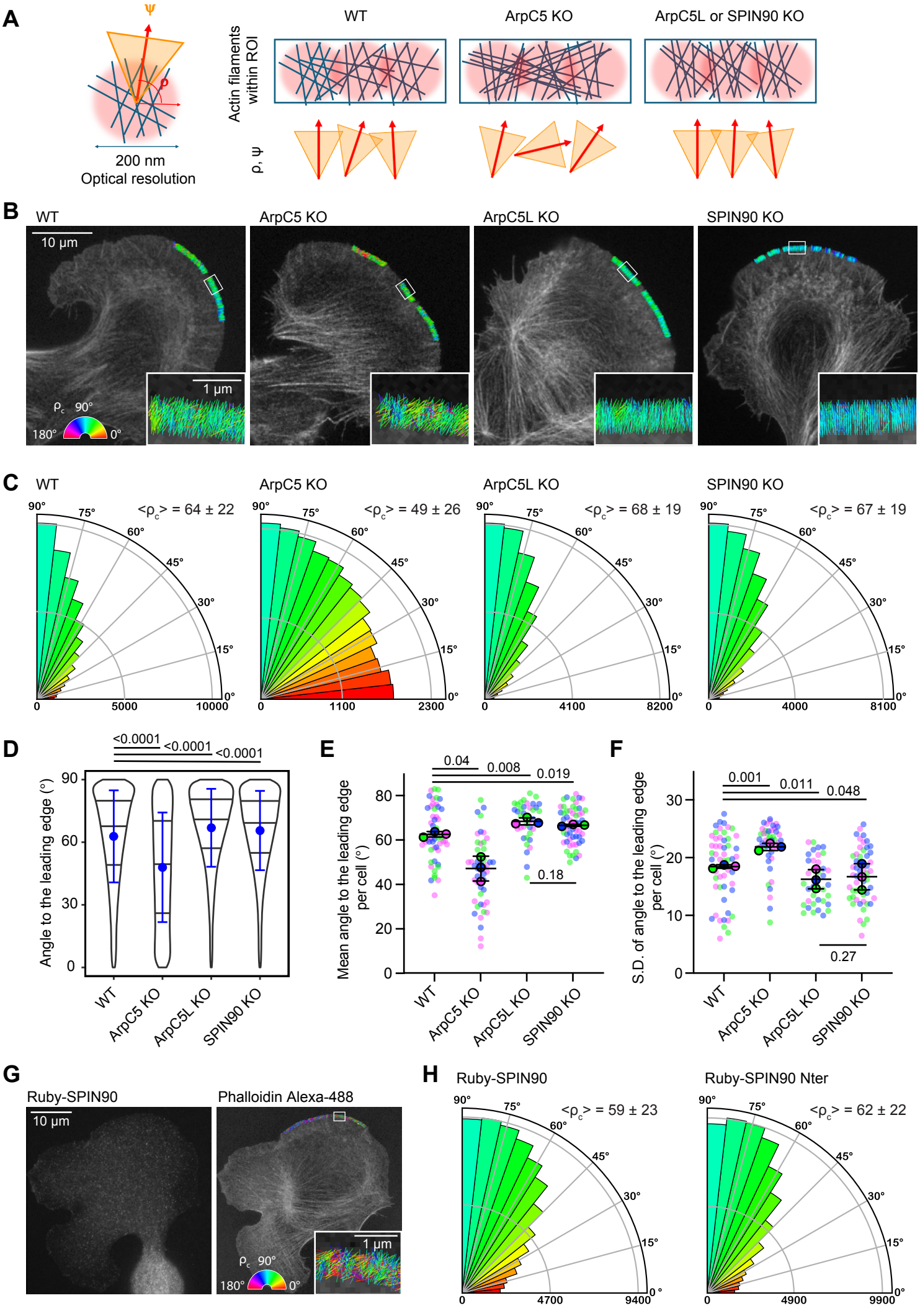
A
ψ
ρ
200 nm
Optical resolution
WT
ArpC5 KO
ArpC5L or SPIN90 KO
Actin filaments within ROI
ρ, ψ
B
WT
ArpC5 KO
ArpC5L KO
SPIN90 KO
10 µm
1 µm
ρc 90°
180°
0°
C
WT
ArpC5 KO
ArpC5L KO
SPIN90 KO
<ρc> = 64 ± 22
<ρc> = 49 ± 26
<ρc> = 68 ± 19
<ρc> = 67 ± 19
90°
75°
60°
45°
30°
15°
0°
0
5000
10000
1100
2300
4100
8200
4000
8100
D
<0.0001
<0.0001
<0.0001
Angle to the leading edge (°)
90
60
30
0
WT
ArpC5 KO
ArpC5L KO
SPIN90 KO
E
0.04
0.008
0.019
0.18
Mean angle to the leading edge per cell (°)
80
60
40
20
0
WT
ArpC5 KO
ArpC5L KO
SPIN90 KO
F
0.001
0.011
0.048
0.27
S.D. of angle to the leading edge per cell (°)
30
20
10
0
WT
ArpC5 KO
ArpC5L KO
SPIN90 KO
G
Ruby-SPIN90
Phalloidin Alexa-488
10 µm
1 µm
ρc 90°
180°
0°
H
Ruby-SPIN90
Ruby-SPIN90 Nter
<ρc> = 59 ± 23
<ρc> = 62 ± 22
90°
75°
60°
45°
30°
15°
0°
0
4700
9400
4900
9900

Figure 6

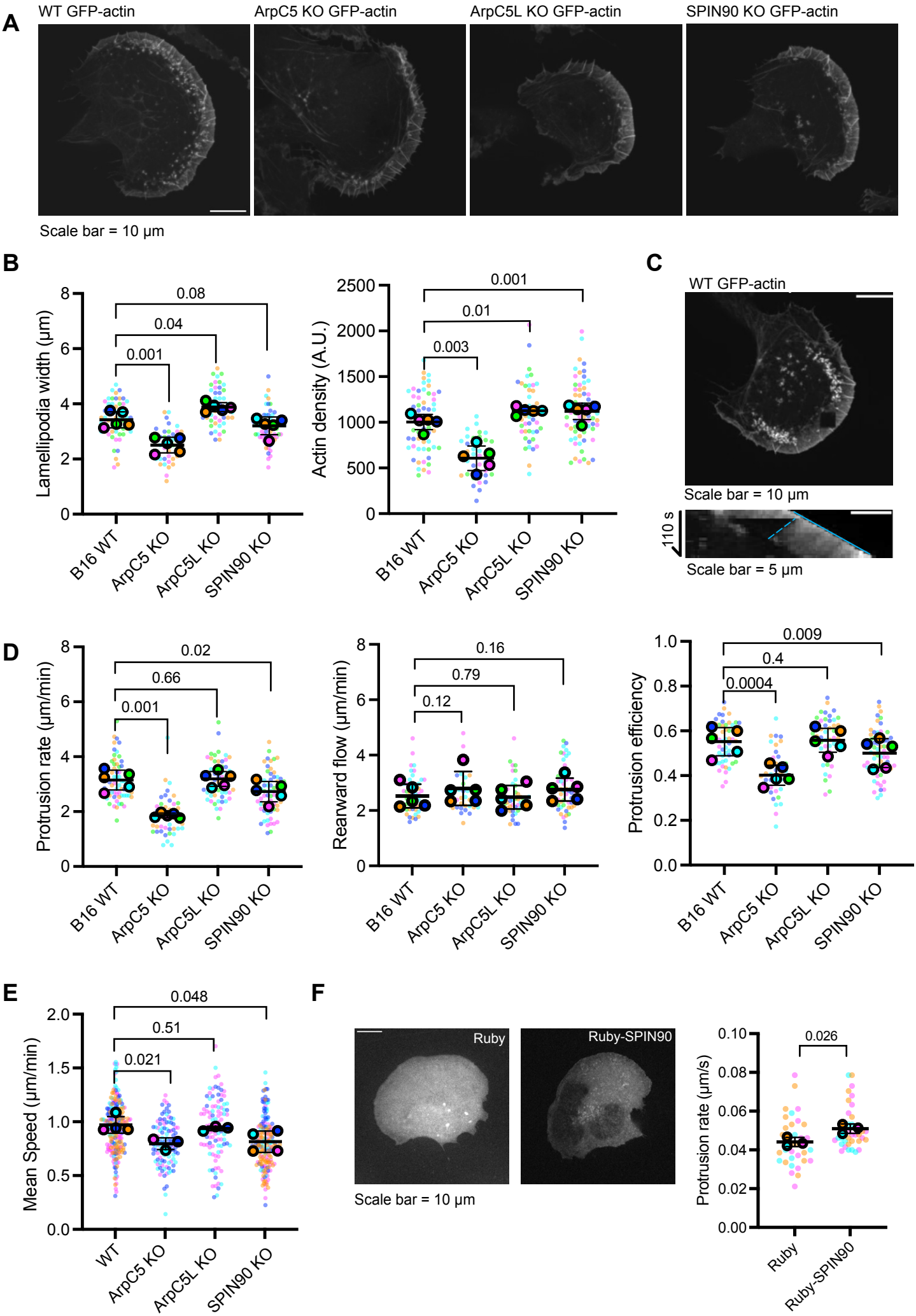
A
WT GFP-actin
ArpC5 KO GFP-actin
ArpC5L KO GFP-actin
SPIN90 KO GFP-actin
Scale bar = 10 µm
B
Lamellipodia width (µm)
0.08
0.04
0.001
Actin density (A.U.)
0.001
0.01
0.003
B16 WT
ArpC5 KO
ArpC5L KO
SPIN90 KO
C
WT GFP-actin
Scale bar = 10 µm
110 s
Scale bar = 5 µm
D
Protrusion rate (µm/min)
0.02
0.66
0.001
Rearward flow (µm/min)
0.16
0.79
0.12
Protrusion efficiency
0.009
0.4
0.0004
E
Mean Speed (µm/min)
0.048
0.51
0.021
WT
F
Ruby
Ruby-SPIN90
Scale bar = 10 µm
Protrusion rate (µm/s)
0.026

Figure 7

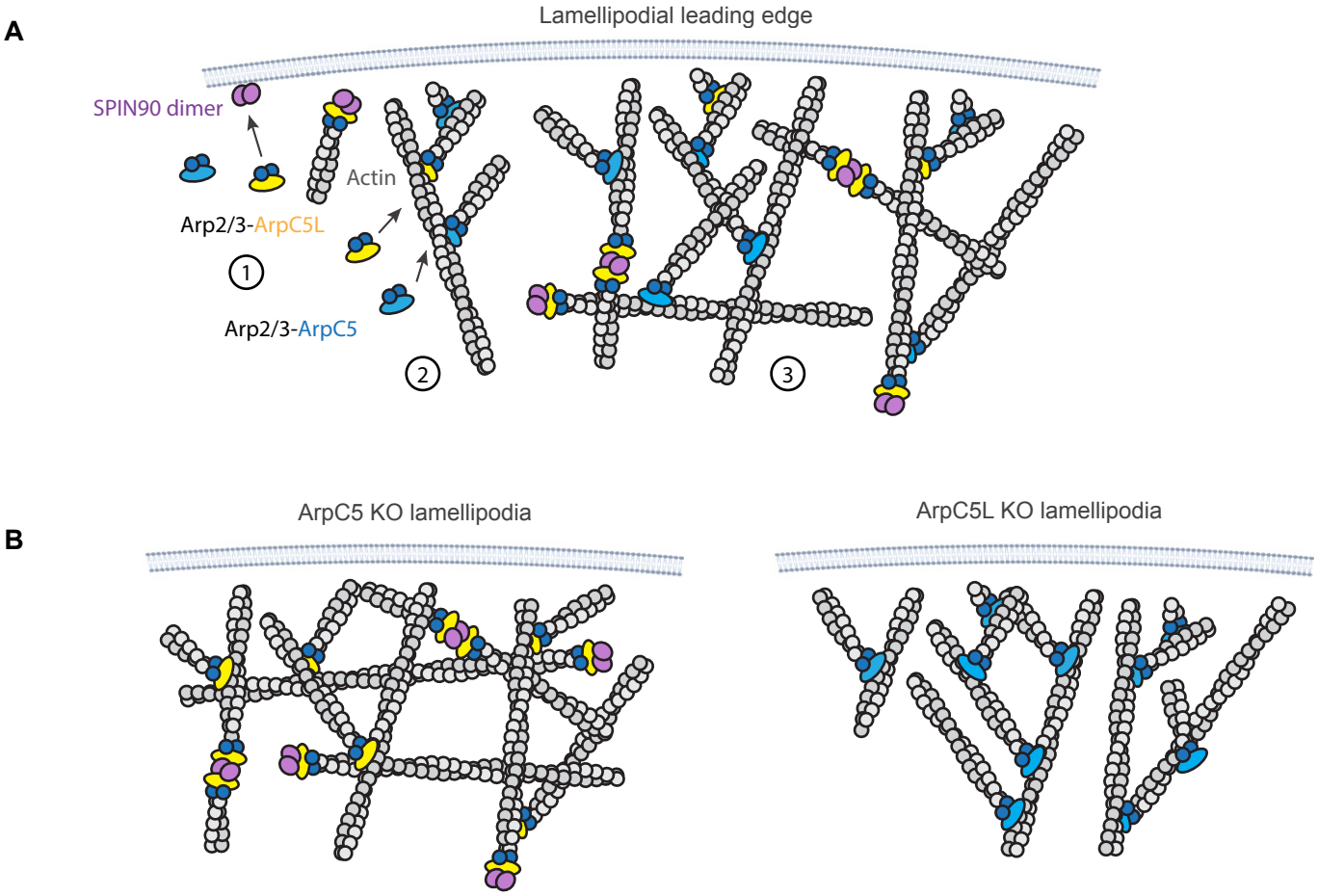
A
Lamellipodial leading edge
SPIN90 dimer
Actin
Arp2/3-ArpC5L
1
Arp2/3-ArpC5
2
3
B
ArpC5 KO lamellipodia
ArpC5L KO lamellipodia

Figure 8